Test beam analysis of ultra-thin hybrid pixel detector assemblies with Timepix readout ASICs

N. Alipour Tehrani[*‡], M. Benoit[†], D. Dannheim[*], E. Firu[§], S. Kulis[*], S. Redford[*], E. Sicking[*]

[*] *CERN, Switzerland,* [†] *Université de Genève, Switzerland,* [‡] *ETH Zürich, Switzerland,* [§] *ISS, Romania*

Abstract

The requirements for the vertex detector at the proposed Compact Linear Collider imply a very small material budget: less than 0.2% of a radiation length per detection layer including services and mechanical supports. We present here a study using Timepix readout ASICs hybridised to pixel sensors of $50 - 500\,\mu$m thickness, including assemblies with $100\,\mu$m thick sensors bonded to thinned $100\,\mu$m thick ASICs. Sensors from three producers (Advacam, Micron Semiconductor Ltd, Canberra) with different edge termination technologies (active edge, slim edge) were bonded to Timepix ASICs. These devices were characterised with the EUDET telescope at the DESY II test beam using 5.6 GeV electrons. Their performance for the detection and tracking of minimum ionising particles was evaluated in terms of charge sharing, detection efficiency, single-point resolution and energy deposition.

1. Introduction

The Compact Linear Collider (CLIC) is a possible future high energy physics project which would provide e^+e^- collisions at centre-of-mass energies up to 3 TeV [1]. This would enable high-precision studies of the Higgs boson, top quark and electroweak physics, in addition to possible new physics beyond the Standard Model [2].

The CLICdp collaboration is performing R&D into detector technologies suitable for such a collider, including fine-grained calorimetry to facilitate particle-flow reconstruction and extremely low material tracking systems to provide high-precision measurements of traversing particles in both space and time.

The requirements of the vertex detector are such as to enable the efficient tagging of displaced vertices in a challenging environment of high occupancy and with stringent limits on heat dissipation and material [3]. For precise tracking, the single-point resolution of each detection layer should be 3 μm. In order to minimise multiple-scattering in the inner detector region, the total material budget of the vertex detector is required to be less than 0.2% of a radiation length per detection layer. This drives the development of extremely thin detectors, currently planned to be 50 μm thick ASICs bonded to 50 μm thick silicon wafers. To reduce the material necessary for cooling, a forced-air-flow system is envisaged. This limits the power dissipation in the vertex detector to $50 \, \mathrm{mWcm}^{-2}$, which leads to a power-pulsing strategy for the readout ASICs [4]. To limit the maximum occupancy in the forward layers to 3%, and to attain the 3 μm single-point resolution, a pixel size of approximately 25 μm × 25 μm is required. Time slicing of 10 ns is necessary in order to separate tracks of interest from the background of overlapping events.

As part of the R&D programme for the CLIC vertex detector, Timepix ASICs [5] have been used as a test vehicle to quantify the performance of thin silicon sensors. The Timepix ASIC reads out 256 × 256 pixels of 55 μm × 55 μm, and has a native thickness of 700 μm. A 14 bit counter is implemented in each pixel. It can be operated either in Time Over Threshold (TOT) mode, in which the counter is incremented continuously as long as the signal is over threshold, or Time Of Arrival (TOA) mode, in which the counter is incremented continuously from the arrival of the first hit until the end of the shutter.

Despite the Timepix ASIC not matching the requirements for the CLIC vertex detector, in combination with sensors of thickness $50 - 500$ μm it can give useful information on the level of charge sharing, detection efficiency and single-point resolution achievable with such hybrid pixel detector technology. Experimental results will validate simulation, which can be used for example to extrapolate to smaller pixel sizes. This note documents the results from the test beam campaign using assemblies of sensors with Timepix readout ASICs. Sections 2 and 3 detail the assemblies and their characterisation. Section 4 describes the experimental setup of the test beam. Section 5 explains the reconstruction process and the data samples available, and Section 6 presents the experimental results.

2. Timepix Assemblies

A summary of the assemblies used in this analysis is shown in Table 1. The reference frame of the assemblies is arranged such that row 0 is the row closest to and parallel with the periphery of the readout ASIC. With the periphery at the bottom, columns are numbered from left to right when viewing the assembly from the sensor side.

2.1. Nominal operating conditions

Nominal values for the threshold and bias voltage were determined to ensure performant operation. Table 2 shows the nominal operating threshold and bias voltage for each assembly, used throughout the following analysis except in the case of a threshold or bias voltage scan. Other relevant parameters and settings include:

Table 1: Details of the different assemblies used in this analysis.

	Sensor				ASIC
Assembly	Producer	Thickness [µm]	Type	Edge	Thickness [µm]
A06-W0110	Advacam	50	p-in-n	20 µm active	700
C04-W0110	Advacam	50	p-in-n	50 µm active	700
C06-W0126	Micron	100	p-in-n	slim edge	100
D05-W0126	Micron	100	p-in-n	slim edge	100
D09-W0126	Micron	100	p-in-n	slim edge	100
L04-W0125	Micron	100	p-in-n	slim edge	700
D04-W0125	Micron	150	n-in-p	slim edge	700
D05-W0125	Micron	150	n-in-p	slim edge	700
D08-W0125	Micron	150	n-in-p	slim edge	700
B06-W0125	Micron	200	n-in-p	slim edge	700
B07-W0125	Micron	300	p-in-n	slim edge	700
C07-W0125	Micron	300	p-in-n	slim edge	700
D03-W0170	Canberra	500	p-in-n	slim edge	700

Table 2: Nominal operating threshold in DAC and energy (where measured [6]), nominal operating bias voltage and leakage current (at operating temperature T) for each assembly.

Assembly	Threshold [DAC]	Threshold [keV]	Bias [V]	Leakage [nA] (T [$^{\circ}$C])
A06-W0110	329	3.077 ± 0.033	15	280 (38)
C04-W0110	405	3.102 ± 0.030	15	220 (37)
C06-W0126	380	-	35	680 (34)
D05-W0126	455	-	35	34,000 (33)
D09-W0126	406	-	35	290 (28)
L04-W0125	410	3.303 ± 0.023	35	760 (39)
D04-W0125	420	-	-35	-380 (35)
D05-W0125	440	-	-35	-350 (34)
D08-W0125	370	-	-35	-410 (35)
B06-W0125	435	3.836 ± 0.057	-50	-580 (33)
B07-W0125	405	-	40	3500 (28)
C07-W0125	435	-	70	-
D03-W0170	370	-	250	870 (28)

- the Timepix ASICs were operated in TOT mode, to provide a measurement related to energy. For some assemblies, a calibration was performed (see Section 3.2).

- the I_{krum} DAC was set to 1, corresponding to the slowest possible return to baseline of the preamplifier output signal and therefore the highest accuracy of the TOT energy measurement.

- the TOT clock frequency used is 96 MHz.

3. Assembly Characterisation

3.1. Assembly quality

The quality of the assemblies was tested in the lab using radioactive sources, under the nominal operating conditions described in Section 2.1. Pixels which were dead or extremely noisy (noise levels 5σ higher than other pixels) were identified and masked for the rest of the data taking. Table 3 shows the numbers of masked pixels per assembly. The total number of masked pixels never exceeds 1.2% of the matrix. Figure 1 shows an example of a masked pixel map, in this case for assembly L04-W0125. This is typical of the masked pixel map for most assemblies, with isolated masked pixels distributed evenly throughout the matrix and on occasion a whole column masked. The masked pixel maps of other assemblies can be seen in Appendix A, Figure 29. The only assembly which does not follow this behaviour is assembly D09-W0126, which requires multiple neighbouring pixels to be masked (see Figure 29(1)).

Table 3: The number of masked pixels for each assembly.

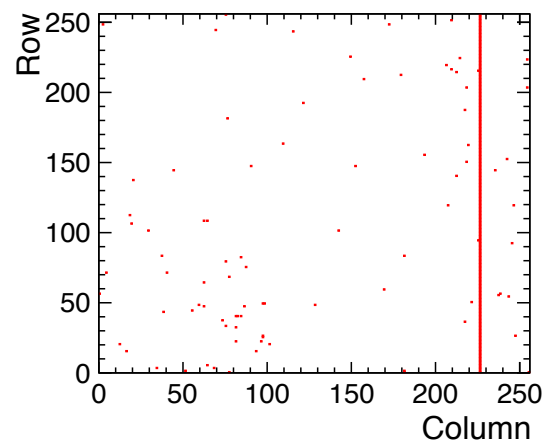| Assembly	# masked pixels (%)
A06-W0110	8 (0.01%)
C04-W0110	493 (0.75%)
C06-W0126	316 (0.48%)
D05-W0126	277 (0.42%)
D09-W0126	293 (0.45%)
L04-W0125	344 (0.52%)
D04-W0125	30 (0.05%)
D05-W0125	33 (0.05%)
D08-W0125	47 (0.07%)
B06-W0125	789 (1.20%)
B07-W0125	394 (0.60%)
C07-W0125	37 (0.06%)
D03-W0170	418 (0.64%)

Figure 1: Masked pixel map, assembly L04-W0125.

Pixels which died after the maps were defined can be identified as pixels which never fire during later data taking - statistically extremely unlikely for a good pixel. The combined test beam data samples were used to determine that no pixels became dead after the maps were defined. This demonstrates the robustness of the assemblies, given proper handling.

Changes in operating conditions or the environment of the assembly can cause additional, non-masked pixels to become noisy (or 'hot') during data taking. To ensure these pixels do not affect the analysis results, hot pixels are also searched for and excluded on a run-by-run basis, see Section 5.2.1.

3.2. Assembly calibration

Six of the assemblies used in this test beam analysis were calibrated, an analysis which is documented elsewhere [6]. Due to the non-linearity of the Timepix charge pre-amplifier, the TOT-energy relationship was modeled as a hyperbola. The function used to parametrise the TOT-energy relationship is called a 'surrogate function' and is defined as:

$$\mathrm{TOT} = aE + b - \frac{c}{E - t} \,, \tag{1}$$

where TOT denotes Time Over Threshold, E denotes energy and a, b, c, t are parameters unique to each calibration [7]. A summary of the global calibration constants found for each assembly is shown

in Table 4. These constants are applied to TOT measurements in this test beam analysis to calculate the energy deposited in the sensor (more details in Section 6.5).

Table 4: Global calibration constants a, b, c, t for each assembly.

Assembly	a [1/96 MHz keV $^{-1}$]	b [1/96 MHz]	c [1/96 MHz keV]	t [keV]
A06-W0110	12.8 ± 1.4	399 ± 60	2104 ± 690	-1.7 ± 1.1
C04-W0110	14.6 ± 1.3	289 ± 50	869 ± 388	0.5 ± 0.9
D09-W0126	17.5 ± 2.0	450 ± 93	1132 ± 1024	1.7 ± 2.7
L04-W0125	15.4 ± 1.6	414 ± 68	2026 ± 733	-1.0 ± 1.1
B06-W0125	30.8 ± 2.4	484 ± 82	1301 ± 515	1.7 ± 0.7
B07-W0125	14.1 ± 2.0	406 ± 114	2148 ± 1981	-1.4 ± 4.4

4. Test Beam Experimental Setup

4.1. EUDET telescope

A beam telescope was used to reconstruct the tracks of the particles passing through the assembly under test. This allows the information from the assembly (hit detection, hit position) to be compared to the extrapolated track position at the assembly, and enables the detection efficiency and hit resolution of the assembly to be calculated.

The EUDET telescope is a high resolution, fast readout beam telescope based on monolithic active pixel sensors [8]. It consists of six Mimosa26 telescope planes [9], whose positions may be adjusted to obtain the optimal tracking resolution. The pixel pitch is 18.4 µm, and the single-point resolution of each plane is ~ 3.5 µm. Scintillators placed in front and behind the telescope act as track triggers. DAQ capabilities are provided by the EUDAQ software framework [10].

4.2. Experimental setup at the DESY II test beam

Test beam line 24 at the DESY II accelerator was used [11]. This beam-line provides electrons of $1 - 6$ GeV, with an energy spread of $\sim 5\%$ and a divergence of ~ 1 mrad. For the analyses presented here, a beam energy of 5.6 GeV was used. Particle rates of several hundred electrons per cm^2 per second were obtained.

To take data at the DESY II test beam, the assembly under test (mounted on a printed circuit board) was inserted from the side into the telescope, between the third and fourth planes (see Figure 2). For most measurements, the assembly was oriented perpendicular to the beam. During angle scans the assembly was rotated to give various angles of incidence between the beam and the detection surface. The planes of the telescope were arranged so as to give the best tracking resolution given the expected levels of multiple scattering for the particular beam energy. At the DESY II test beam, this corresponded to having the third and fourth planes as close to the assembly under test as possible, the first and last planes as far away as possible ($\sim \pm 30$ cm), and the second and fifth places spaced equally in between. In this configuration, the expected position resolution of the extrapolated track is ~ 3.0 µm.

The coordinate system of the test beam is right-handed, with $+z$ in the direction of the beam (from right to left in Figure 2), x in the horizontal direction and y in the vertical direction. The assemblies are mounted on the PCB in such a way that the periphery is nearest the readout connection, so rows of pixels are oriented vertically and columns horizontally. Results including tracks from the telescope are presented in the reference frame of the telescope, where x measures row number and y measures column number.
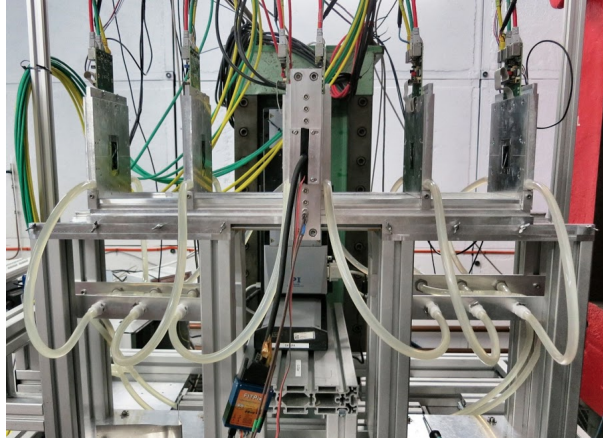
Figure 2: The DESY II test beam setup, showing the assembly (centre, inserted horizontally with FITPix connection shown) and the six telescope planes (three on either side of the assembly).

4.3. Experimental setup at the CERN PS test beam

The majority of the data samples used in this study were recorded at the DESY II test beam, as detailed above. However, a small additional data sample for assembly C07-W0125 was recorded at the CERN PS test beam. Here, the assembly was inserted into the telescope from the bottom, due to a different mechanical stage being used. In addition, the telescope planes were positioned differently due to the 10 GeV beam energy. To minimise the tracking resolution, the three planes on either side of the assembly were brought as close to the assembly as possible. In this configuration, the expected position resolution of the extrapolated track is $\sim 2.8\,\mu m$.

4.4. Data readout

The printed circuit board containing the assembly was connected to a FITPix device [12], which provides low voltage to the Timepix ASIC, reads out signals and controls the data acquisition. An external high-voltage power supply was used to bias the sensor. Both the FITPix and the high-voltage power supply were controlled from a PC.

In order to increase the rate of data taking, a Man-in-the-Middle Trigger Logic Unit (MiM-TLU) was used [13]. It was configured to keep the Timepix shutter open during 15 triggered Mimosa shutters of 230 µs each. The data from each Timepix frame was then copied 15 times and combined with each of the 15 Mimosa frames.

5. Reconstruction and Data Samples

Two software frameworks are used to reconstruct the test beam data samples. The first, `EUTelescope` [14], is used to reconstruct the tracks from the telescope. The second, `pyEudetAnalysis`, is used to reconstruct the hits in the assembly and perform the rest of the analysis presented in this study. The software for `pyEudetAnalysis` can be found in a dedicated GitHub directory [15].

5.1. Track reconstruction

Tracks in the telescope are reconstructed with the `EUTelescope` software, which uses several processors within the Marlin framework [16] to turn the raw files into LCIO files and ROOT trees. In the

first part of the reconstruction, a subset of the run is used to calculate the alignment of the six telescope planes. The steps are as follows:

1. the **converter** processor, which turns the raw file into an slcio file and removes the hot pixels from each telescope plane

2. the **clusearch** processor, which clusters the hits in each telescope plane

3. the **hitmaker** processor, which reconstructs a hit position for each cluster

4. the **align** processor, which assumes straight tracks to align the six telescope planes relative to each other

In the second part of the reconstruction, the full run and the alignment are used to reconstruct the tracks:

1. the **converter** processor, as before

2. the **clusearch** processor, as before

3. the **hitmaker** processor, as before

4. the **fitter** processor, which takes into account the positions of all six telescope planes, the hits in each plane and the material of all planes to make a fit for each track. Figure 3 shows the track χ^2/NDF for three different runs. A cut is applied to remove the 5% of tracks with the highest χ^2/NDF.

For more details of these steps, see [14]. The resulting ROOT file contains two trees (one for track information, one for assembly information). The extrapolated track position is recorded at the position of each layer of the telescope, and at the position of the assembly. The pixel maps detected by the assembly are also recorded. This file is the input to the `pyEudetAnalysis` software, which performs the rest of the reconstruction and analysis.
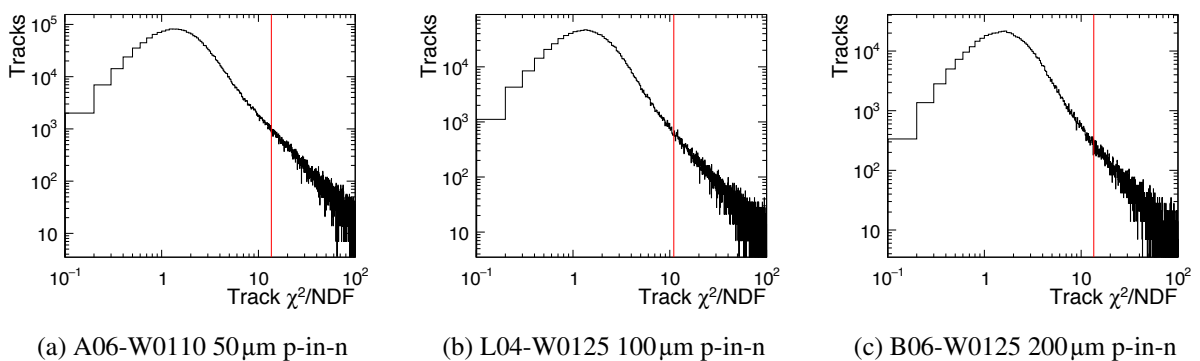

| (a) A06-W0110 50 μm p-in-n | (b) L04-W0125 100 μm p-in-n | (c) B06-W0125 200 μm p-in-n |

Figure 3: Track χ^2/NDF for three different runs. A cut (red line) is applied to remove the 5% of tracks with the highest χ^2/NDF.

5.2. Assembly hit-map reconstruction

5.2.1. Hot pixel determination

Hot pixels are pixels which fire so often that they do not reliably indicate the passage of a charged particle through the assembly. They may be 'noisy' pixels which just avoided the masking threshold (see

Section 3.1), or they may be pixels which are adversely affected by the deposition of charge in them or the assembly in general. Hot pixels can be created by manufacturing errors and physical defects in the assembly. They are detrimental to the performance of the assembly. Therefore, a threshold is set on the firing frequency of each pixel. Pixels which fire with a frequency higher than this threshold are said to be hot, and are then masked in the matrix of hit pixels. This mask is applied in addition to the initial mask determined before the test beam period (Section 3.1).

In this analysis, hot pixels are defined as pixels which fire more than once for every 100 frames recorded. Figure 4 shows how this threshold compares to the measured pixel firing frequency for three different assemblies under nominal operating conditions. Depending on the assembly and operating conditions, the most-likely pixel firing frequency is around 10^{-3}. In order to achieve a statistically accurate determination of the pixel firing frequency, a large number of frames must be studied.

(a) L04-W0125 $100\,\mu$m p-in-n   (b) D03-W0170 $500\,\mu$m p-in-n   (c) C07-W0125 $300\,\mu$m p-in-n
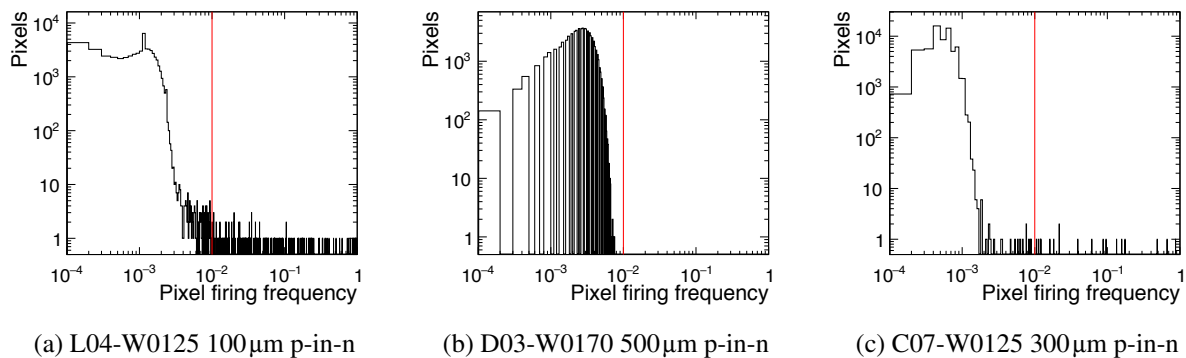
Figure 4: The measured firing frequency of each pixel in three different assemblies, recorded under nominal operating conditions. The hot pixel threshold is defined as 10^{-2} (red line).

A toy study was performed to determine the number of frames which should be studied in order for the probability of labeling a pixel as 'hot' due to a statistical fluctuation to drop below the level of one pixel in the assembly. The toy study was set up to randomly generate a certain number of frames. Each frame consists of 60 'hits' being randomly distributed amongst 65,536 pixels. This number of hits is typical for data samples recorded at the test beam. The number of pixels which fire with a frequency higher than 0.01 are recorded. The toy experiment is repeated 1,000 times, and the mean number of 'hot' pixels determined. Figure 5 shows the number of hot pixels as a function of the number of unique frames considered. The 'step' pattern is due to the interplay between the threshold, the number of frames considered and the discrete nature of a hit. Since no pixels were simulated to be hot in the toy study, the number approaches zero for a sufficient number of considered frames. It was determined that at least 600 unique frames should be used to determine the hot pixels in a run. Most runs contain at least this many frames. In order to get the most statistically accurate result possible, all frames in a run are used to determine the hot pixels. Figure 6 shows the number of hot pixels as a function of the number of frames considered in a test beam run. A similar pattern to that shown in Figure 5 is found, except in this instance a number of 'true' hot pixels exist. Note that the 'number of frames considered' does not equate to the number of unique frames, due to the MiM-TLU (see Section 4.4). There is approximately a factor of 15 between the number of data 'frames' and the number of unique pixel frames.

Under nominal operating conditions the hot pixels of an assembly from one run to the next are closely correlated. Figure 7(a) shows the identity of hot pixels in sensor A06-W0110, as a function of run number. Approximately the same set of pixels is hot throughout data taking, over a time period of months. However, pixels can also become hot or cease to be hot over time. This could be due to environmental conditions (such as temperature) in addition to small unintended changes in the operating conditions of the chip (threshold move). The same behaviour is shown in Figures 7(b) and 7(c). Due to
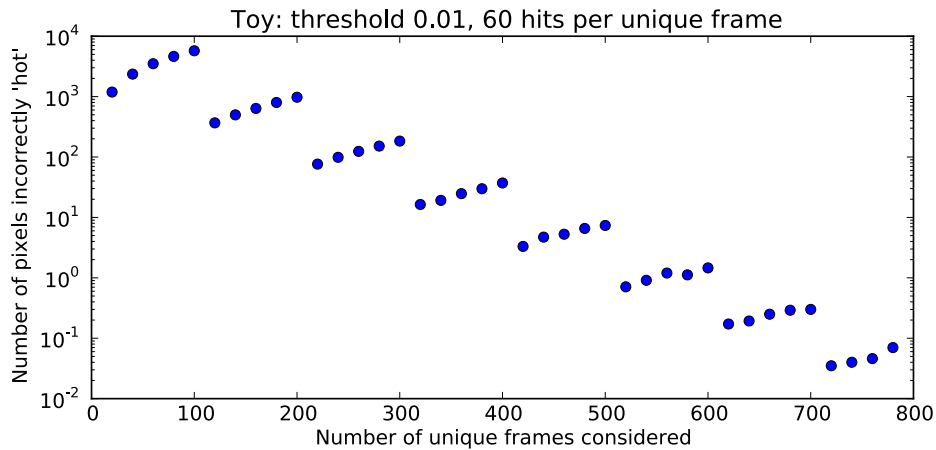
Figure 5: Plot produced in a simulated toy study, showing the number of pixels incorrectly labeled as hot due to statistical fluctuations as a function of the number of unique frames considered.
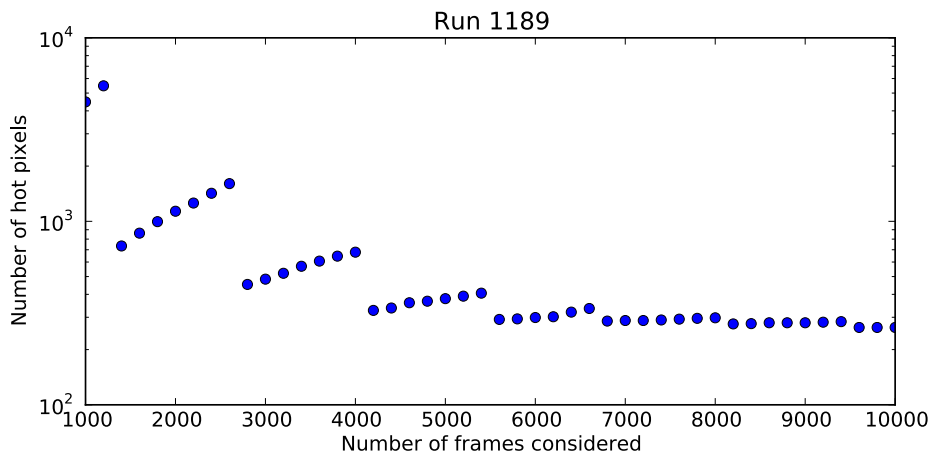

Figure 6: The number of pixels labeled as hot as a function of the number of frames considered for a data run. Assembly L04-W0125.

this variation in hot pixels from run to run, it was decided that each run should determine its own hot pixels, rather than making an average or sum over all runs. To give an impression of the level of hot pixels per assembly, Table 5 shows the average number of hot pixels per run for each assembly under nominal operating conditions. Figure 8 shows the pixel firing frequency of a typical hot pixel map, recorded by assembly L04-W0125 under nominal operating conditions. The hot pixels are seen to be isolated and distributed across the whole matrix. Assembly B07-W0125 has an unusually large number of hot pixels. It is thought that the threshold on this assembly was set too close to the noise, and that slight variations in operating or environmental conditions caused many non-masked pixels to become noisy.

The number of hot pixels depends strongly on the operating conditions, as demonstrated in threshold and bias voltage scans. Figure 9(a) shows the number of hot pixels as a function of threshold. It shows that the number of pixels defined as 'hot' increases dramatically as the threshold DAC value increases (for this p-in-n sensor), which allows smaller signals to be recorded. The number of hot pixels found per run as a function of bias voltage is shown in Figure 9(b). At very low bias voltage, the number of

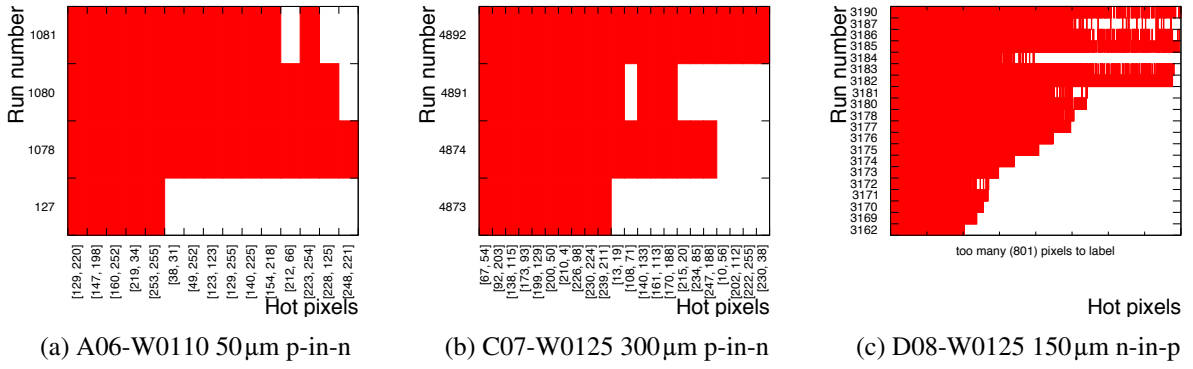(a) A06-W0110 50 µm p-in-n   (b) C07-W0125 300 µm p-in-n   (c) D08-W0125 150 µm n-in-p

Figure 7: The identity of hot pixels for different runs recorded under nominal operating conditions.

Table 5: The average number of hot pixels per run under nominal operating conditions for each assembly.

Assembly	Avg # hot pixels
A06-W0110	11.5
C04-W0110	0.1
C06-W0126	10.7
D05-W0126	0.3
D09-W0126	0.3
L04-W0125	239.6
D04-W0125	0.0
D05-W0125	40.0
D08-W0125	442.7
B06-W0125	12.8
B07-W0125	4371.0
C07-W0125	16.0
D03-W0170	0.0
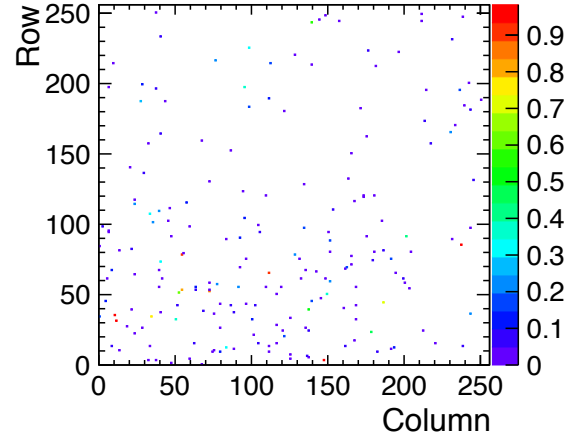
Figure 8: Hot pixel map, assembly L04-W0125. The colour scale shows the firing frequency of the hot pixels.

hot pixels increases due to the increased electronics noise from the higher input capacitance. These two results further corroborate that the hot pixels should be determined per run, to take into account changes in operating conditions of the assembly. Further examples are shown in Figure 30 of Appendix B.

5.2.2. Clustering

The pixels which fired in each frame (with the hot pixels now removed) are clustered. The clustering algorithm employed is the SciPy hierarchical `fclusterdata` [17], which determines how to form clusters from hit pixels with a distance criterion. The result of clustering with different distance criteria is shown in Figure 10. A distance criterion of 1 forms clusters from hit pixels which share a common edge. A distance criterion of $\sqrt{2}$ forms clusters from hit pixels which share a common corner or a common edge. A distance criterion of 2 forms clusters from hit pixels sharing edges or corners, or with one 'skipped' pixel between them. In this analysis a distance criterion of $\sqrt{2}$ is used, due to the low charge sharing and high detection efficiency of the assemblies.

(a) A06-W0110 50 μm p-in-n
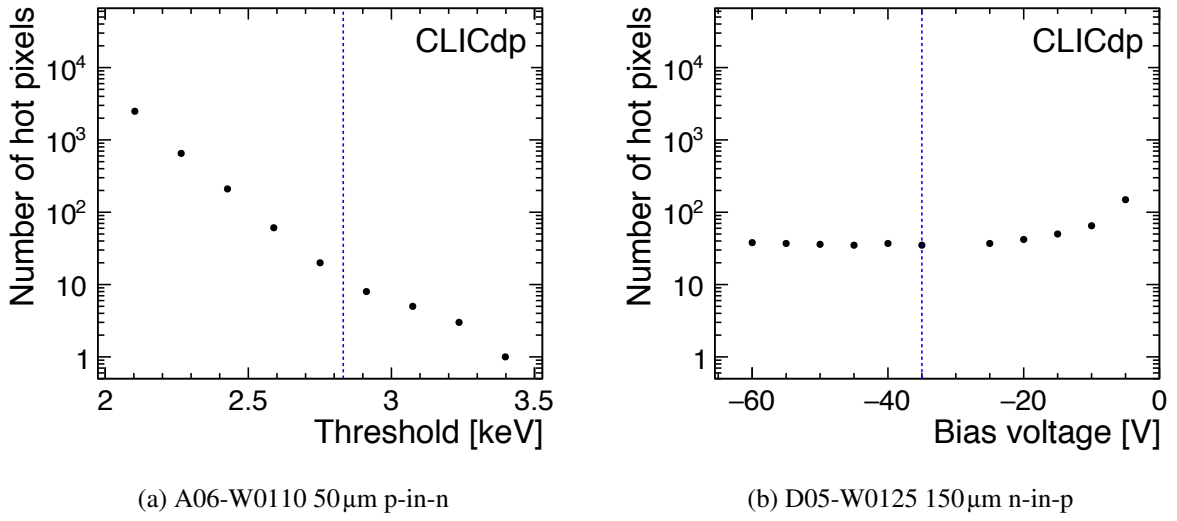
(b) D05-W0125 150 μm n-in-p

Figure 9: The number of hot pixels as a function of operating threshold (a) and bias voltage (b). The nominal operating condition is shown by the blue dashed line.
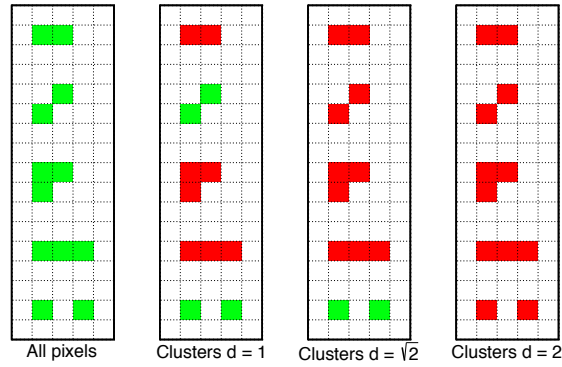

Figure 10: Demonstration of the effect of clustering hit pixels (left) with different distance criteria (d). Hit pixels which form clusters are shown in red, non-clustered hit pixels are shown in green.

5.2.3. Hit position reconstruction

To determine the hit position for each cluster, four methods of hit reconstruction were considered:

- **digital centroid hit position** in which the hit position is reconstructed at the geometric centre of the cluster. This method only uses the binary information of hit pixels, without any knowledge of the charge of the hit pixels.

- **maximum TOT centroid hit position** in which the hit position is reconstructed at the centre of the pixel within the cluster with the highest charge.

- **charge weighted hit position** in which the hit position is reconstructed by using the charges of the hit pixels as weights for a linear weighting to find the centre-of-gravity of the cluster.

11

- **η-corrected hit position** in which the hit position is reconstructed by using the charges of the hit pixels as weights (as for the charge weighted hit position) while taking into account non-linearities in the charge-sharing between pixels [18]. The distance with which the hit position moves from the geometric centre of the two pixels under consideration is defined using the inverse error function, defined as $\text{erf}^{-1}(z)$ where:

$$\text{erf}(z) = \frac{2}{\sqrt{\pi}} \int_0^z e^{-t^2} dt \,. \tag{2}$$

In practice, this is calculated with:

$$shift = \sigma_{EC} \times \texttt{TMath.ErfInverse}(2 \times Q_{rel} - 1)\,, \tag{3}$$

where σ_{EC} is a parameter to be determined and the relative charge Q_{rel} is the charge of the more highly charged pixel divided by the total charge of the pair of pixels, Q_{max}/Q_{total} (see Figure 11). The parameter σ_{EC} depends on several factors, including the thickness of the silicon and the operating conditions of the assembly. It also varies depending on whether TOT or energy is used to calculate the hit position. It can be determined by minimising the two-pixel cluster resolution. In the analysis, a single σ_{EC} is used for calculating shifts in both x and y. It is optimised per run.

The hit reconstruction method used in the analysis depends on the size of the cluster. Clusters of size one are assigned a hit position in the centre of the pixel. The η-correction method is used for two-pixel clusters of all shapes $((1 \times 2), (2 \times 1)$ and $(2 \times 2))$. The η-correction method is also used for four-pixel clusters of shape (2×2), by calculating two shifts considering the two diagonal pairs of pixels. A factor of $\sqrt{2}$ is included to ensure that the same σ_{EC} parameter can be used as in the two-pixel cluster case. The hit position of three-pixel clusters of shape (2×2) is also reconstructed using the η-correction method. Since this method must consider pairs of pixels to calculate the shift, the 'missing' pixel is assigned a charge of 10% of the total cluster charge, and the method proceeds as in the four-pixel cluster case. The choice of 10% is an estimate to take into account charge sharing below threshold, and was not optimised. All other clusters use the charge weighted method to determine their hit position.
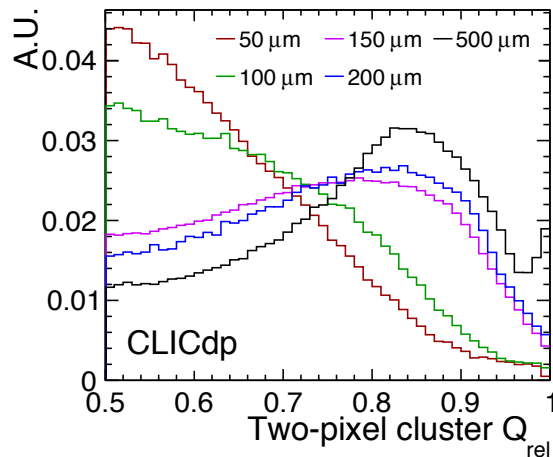

Figure 11: Measured relative charge distribution in two-pixel clusters for various silicon thicknesses. Each histogram is scaled to have unit area.

5.3. Track-hit alignment

The purpose of the alignment process is to determine a set of alignment constants, which when applied to the reconstructed hits from the assembly bring them into line with the extrapolated track positions

from the telescope. The hit positions of the clusters are calculated following the method set out in Section 5.2.3. No selection is made on cluster size or shape. One set of alignment constants is calculated per run. The maximum number of frames used to calculate the alignment constants is limited to 10,000 (to ensure the process is not too computationally intensive). As most runs contain more than this number of frames, a 'skip' is implemented so that only 10,000 frames, equally spread throughout the run, are considered.

The assembly has a total of 6 possible degrees of freedom: translations in x, y and z and rotations about the x, y and z axes. The position of the assembly is fixed by definition at $z = 0$; all measurements of the z positions of the six telescope planes are made relative to this. Additionally the assembly hit positions are extremely insensitive to rotations of the assembly about the x and y axes, since the tracks are perpendicular to the assembly and the assembly is only sensitive in x and y. Therefore only three alignment constants are calculated: for translations in x and y and for rotation about the z axis.

The initial relationship between the tracks and the hits are plotted (see Figure 12(a)) showing a good correlation as expected. However, a small but significant misalignment is present. A pre-alignment procedure is performed, in order to bring the hits roughly into line with the tracks. Since the rotation of the assembly about the z axis is known to be small, the pre-alignment considers only translations in x and y. The difference between the tracks and hits in these two co-ordinates are plotted, as shown in Figures 12(b) and 12(c)). The narrow peaks in these plots correspond to matching track-hit pairs, the broad backgrounds are composed of non-matching pairs from the same frame. From these figures, the centre of the bin with the highest content in each co-ordinate is used as an alignment constant and is applied to the assembly.
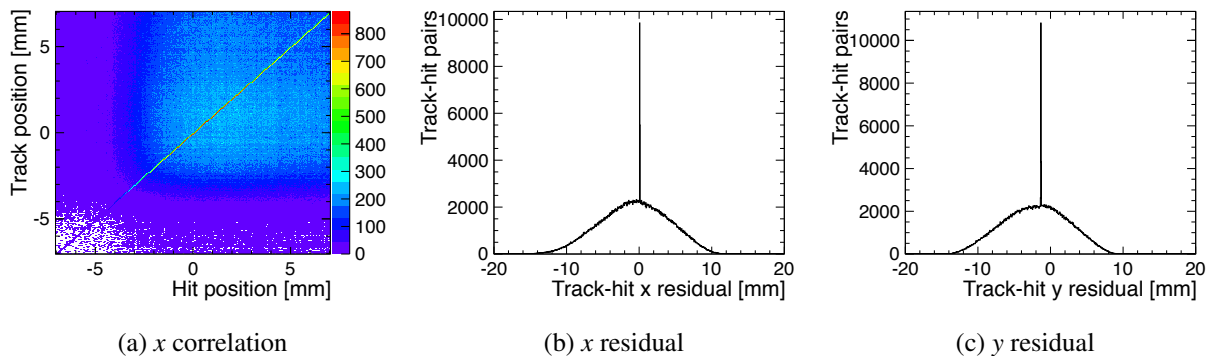

(a) *x* correlation   (b) *x* residual   (c) *y* residual

Figure 12: (a) The pre-alignment correlation between track positions and hit positions in *x*. (b)-(c) The distance between each track and all hits in a frame, for all tracks considered in the alignment. Assembly L04-W0125.

With the tracks and hits now roughly aligned, clusters are filtered to retain only those matching track positions. The distance criterion for filtering is 0.3 mm, larger than usual to allow for the incomplete alignment. Correlation plots (for example Figure 13(a)) show that the 'background' seen previously (in Figure 12(a)) is largely removed by the track matching. This 'background' is caused by tracks being compared to non-matching clusters.

The main alignment procedure is then performed, to precisely align the tracks and the hit positions of matched clusters. The metric used is the sum of the radial distance between each track and the closest hit. If the track-hit distance is more than 0.5 mm, the pair is not considered good and the distance does not contribute to the total. The Nelder-Mead method of SciPy `optimize.minimize` [19] is used to minimise the total distance. This function automatically varies the rotation about z and the x and y translations simultaneously to find the optimal alignment.

The three alignment constants calculated by `optimize.minimize` are applied to the hits, on top

of the two pre-alignment constants. Correlation and residual plots are made to enable the quality of the alignment to be assessed (see Figures 13(b) and 13(c)). The alignment constants are recorded so they may be applied to the hits each time the run is analysed.
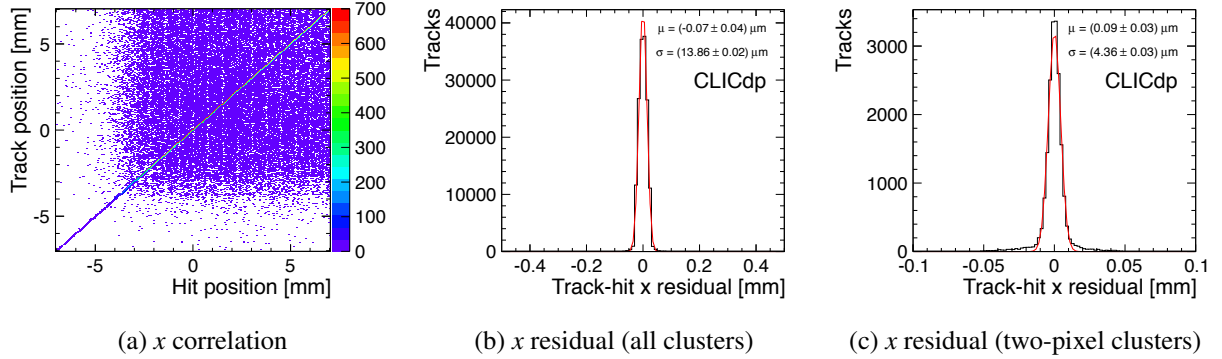

(a) *x* correlation (b) *x* residual (all clusters) (c) *x* residual (two-pixel clusters)

Figure 13: (a) The post-alignment correlation between track positions and hit positions in *x*. (b)-(c) The *x* residual for all and two-pixel clusters. Assembly L04-W0125.

5.4. Track-hit matching

With the reconstructed hit positions from the clusters in the assembly now aligned with the tracks reconstructed by the telescope, the final step is to match hits to tracks. This is achieved by taking the closest hit to each track, within a radial distance of 0.1 mm (see Figure 14). If no hit exists within this distance, the track is left unmatched. Hits which are not matched to tracks are discarded. In this way, the hits used in the following analysis were all caused by the passage of a reconstructed track through the assembly. This allows studies such as hit resolution and energy deposition. Additionally, tracks projected to pass through the assembly allow studies of detection efficiency.
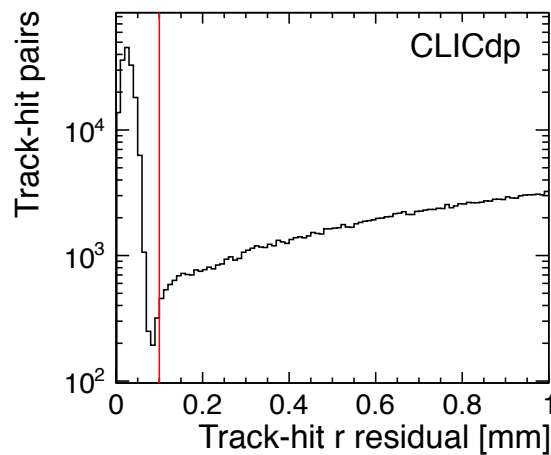

Figure 14: Radial distance between all track-cluster pairs, showing the reason for the 0.1 mm selection (red line). Assembly L04-W0125.

Table 6: Number of runs (million frames) recorded under different operating conditions per assembly.

Assembly	Nominal operating conditions	Bias scan	Threshold scan
A06-W0110	4 (0.8)	13 (3.1)	12 (1.8)
C04-W0110	10 (1.1)	12 (2.8)	27 (4.0)
C06-W0126	7 (0.6)	10 (0.9)	35 (3.6)
D05-W0126	3 (0.2)	10 (1.0)	7 (0.8)
D09-W0126	4 (0.2)	9 (0.4)	8 (0.3)
L04-W0125	7 (0.9)	15 (2.2)	6 (0.8)
D04-W0125	17 (3.0)	9 (1.5)	21 (4.2)
D05-W0125	2 (0.2)	10 (1.6)	17 (3.0)
D08-W0125	20 (2.9)	12 (1.7)	9 (1.9)
B06-W0125	13 (0.9)	13 (0.9)	36 (3.1)
B07-W0125	1 (0.2)	16 (2.4)	0 (0.0)
C07-W0125	4 (0.2)	10 (0.6)	5 (0.3)
D03-W0170	16 (2.4)	5 (3.1)	0 (0.0)

5.5. Data samples

Following the reconstruction procedure detailed above, Table 6 gives details of the data samples available for each assembly. This totals over 400 runs, containing over 50 million frames.

6. Experimental Results

6.1. Effect of track position on charge sharing

The extrapolated hit position of tracks making cluster sizes $1 - 4$ is shown in Figure 15 for an assembly with a $100\,\mu m$ thick sensor. As expected when the tracks are perpendicular to the sensor, multi-pixel clusters are created when the track hits the edge or corner of a pixel, enabling charge sharing between it and the neighbouring pixels. Additional plots of track position for different cluster sizes and sensor thicknesses can be found in Figure 32 of Appendix C. From this instructive figure, the effect of sensor thickness on the formation of multi-pixel clusters is demonstrated.
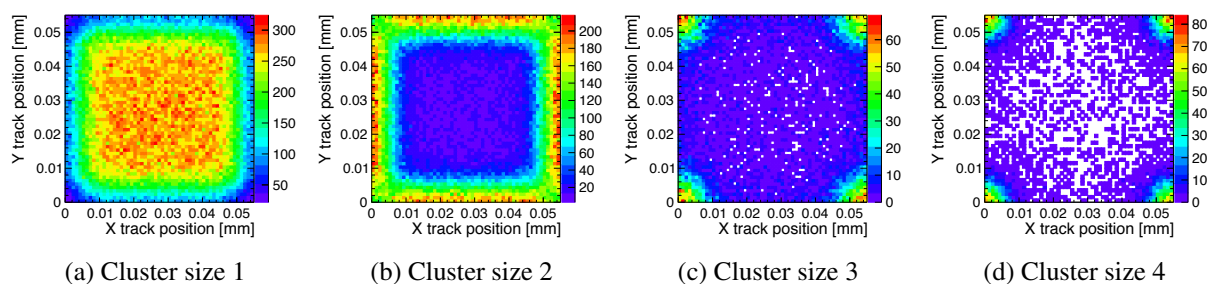

(a) Cluster size 1   (b) Cluster size 2   (c) Cluster size 3   (d) Cluster size 4

Figure 15: Extrapolated track position within the pixel for cluster sizes $1 - 4$. Data recorded with assembly L04-W0125, under nominal operating conditions.

The one-dimensional profile of the two-pixel cluster plots (Figure 15(b) and others) can be compared for different sensor thicknesses, see Figure 16. This further demonstrates how tracks further from the pixel edge can create multi-pixel clusters in thicker sensors.
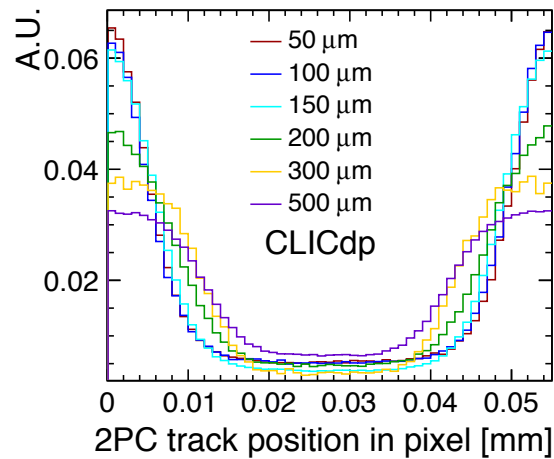
Figure 16: Track position within the pixel for tracks making two-pixel clusters ('2PC') for various sensor thicknesses. Each histogram is scaled to have unit area.

6.2. Cluster size distribution

The distribution of cluster sizes is a direct measure of how much charge-sharing takes place in the sensor. It is expected that thicker sensors will demonstrate more charge-sharing, as the charges have a longer distance to drift and so can diffuse across a larger transverse area. Charge-sharing is not always detected, as the shared charge can be below threshold in the neighbouring pixel. This results in undetected energy deposits.

The cluster size is defined as the number of pixels which are clustered together according to the method described in Section 5.2.2. For sensor thicknesses in the range of $50 - 500\,\mu m$, cluster sizes of one to four are expected due to charge sharing, with neighbouring pixels sharing common edges and not extending more than two pixels in any direction. Larger clusters and clusters of different shapes can occur, but are not consistent with charge-sharing. For instance, δ-rays can cause extremely large clusters. Smaller multi-pixel clusters which do not share common edges (for example, a two-pixel corner-to-corner cluster) can be explained by other effects, such as inefficiencies, hits combined with hot pixels, or clusters affected by dead pixels. It is also possible (though unlikely) that another track (reconstructed or not), or other scattered particle hit an adjacent pixel by chance and cause a multi-pixel cluster. Table 7 details the possible cluster shapes and the most likely phenomena to cause each one.
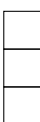
The fraction of different cluster sizes was calculated as a function of sensor thickness for runs recorded under nominal operating conditions, see Figure 17. As expected, charge-sharing increases with sensor thickness. The fraction of single-pixel clusters decreases from 81.5% with a $50\,\mu m$ sensor to 22.8% with a $500\,\mu m$ sensor. As expected for square pixels, the fraction of (2×1)- and (1×2)-pixel clusters is very similar.

The fraction of different cluster sizes also depends on the operating conditions of the assembly. Figure 18(a) shows how the distribution of cluster sizes changes as the bias voltage varies. There are two regimes. For the most part, a stronger bias voltage reduces the amount of charge-sharing because the charges created in the silicon are pulled more strongly in the electric field, and so have less time to diffuse in the transverse direction. However, with very small bias voltages less of the deposited charge is collected (the silicon is under-depleted). An increase in bias voltage in this region increases the charge-sharing, as the pixel neighbouring a hit pixel is more likely to be over threshold as more charge is collected. The same behaviour is seen in other assemblies, see Figures 31(a) and 31(b) of Appendix C.

Figure 18(b) shows how the distribution of cluster sizes changes as the threshold varies. Lowering the

Table 7: Most common cluster shapes and their most likely causes.

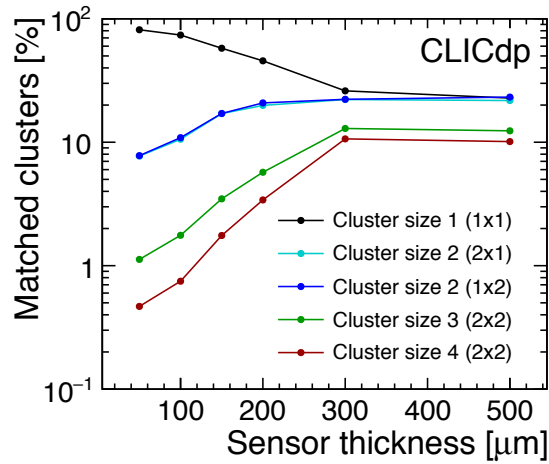| Shape	Cluster size	Size in x	Size in y	Most likely cause
	1	1	1	track
	2	2	1	track + charge-sharing
	2	1	2	track + charge-sharing
	2	2	2	track + charge-sharing + inefficiency or track + hot pixel
	3	2	2	track + charge-sharing
	4	2	2	track + charge-sharing
	≥ 3	≥ 3	≥ 1	track + δ-ray
	≥ 3	≥ 1	≥ 3	track + δ-ray

Figure 17: Fraction of different cluster sizes as a function of sensor thickness for runs recorded under nominal operating conditions.

threshold increases the amount of charge-sharing detected, as the pixel neighbouring a hit pixel is more likely to be above threshold. From other assemblies (see Appendix C, Figures 31(c) and 31(d)) there is evidence that the direction of change reverses below a certain threshold, due to the noise level being reached. At this limit the number of one-pixel clusters increases.

6.3. Single-point resolution

The single-point resolution of the Timepix assemblies can be measured by comparing the calculated hit position (Section 5.2.3) with the extrapolated track position provided by the telescope. This 'residual'

(a) D05-W0125 150 μm n-in-p
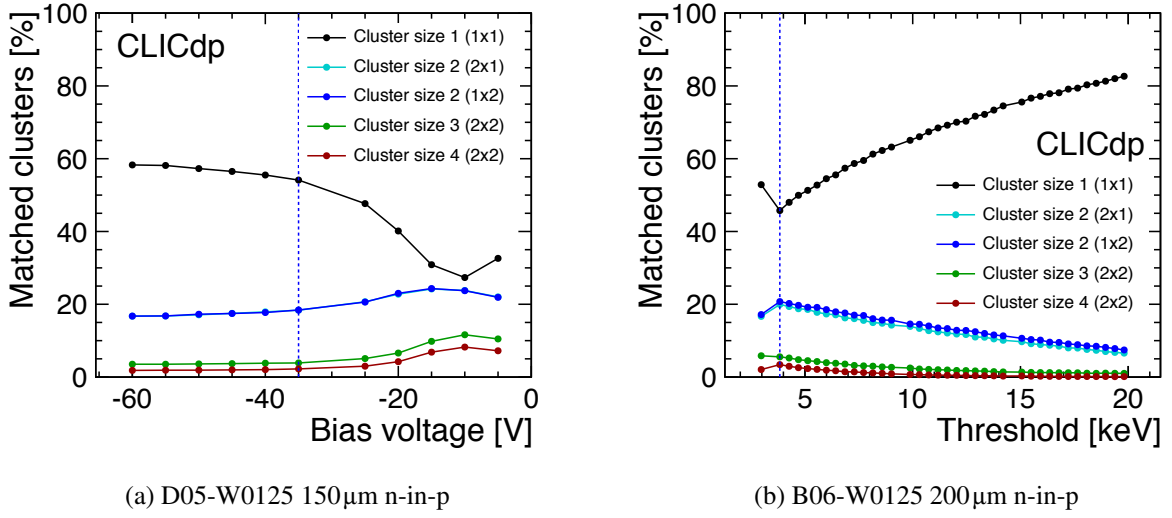
(b) B06-W0125 200 μm n-in-p

Figure 18: Fraction of different cluster sizes as a function of bias voltage (a) and threshold (b). The nominal operating condition is shown by the blue dashed line.

distance contains the single-point (or hit) resolution and the track resolution combined in quadrature:

$$\sigma_{\text{residual}}^2 = \sigma_{\text{hit}}^2 + \sigma_{\text{track}}^2. \tag{4}$$

All figures presented in the section refer to the residual measurement. To obtain an estimate of the single-point resolution, the track resolution (approximately 3 μm at the DESY II test beam) should be unfolded.

Different cluster sizes give different residuals, as shown in Figure 19. This is due to the varying amount of information available to the hit reconstruction method in each case. For single-pixel clusters the geometric centre of the hit pixel is used as the hit position. With no further information, a single-point resolution of pixel pitch/$\sqrt{12}$ is expected [20], close to that seen in Figure 19(a). For multi-pixel clusters where charge sharing has occurred, the hit-position method has much more information available and is able to do an interpolation, as described in Section 5.2.3. This leads to the smaller residuals seen in Figures 19(b) to 19(d).
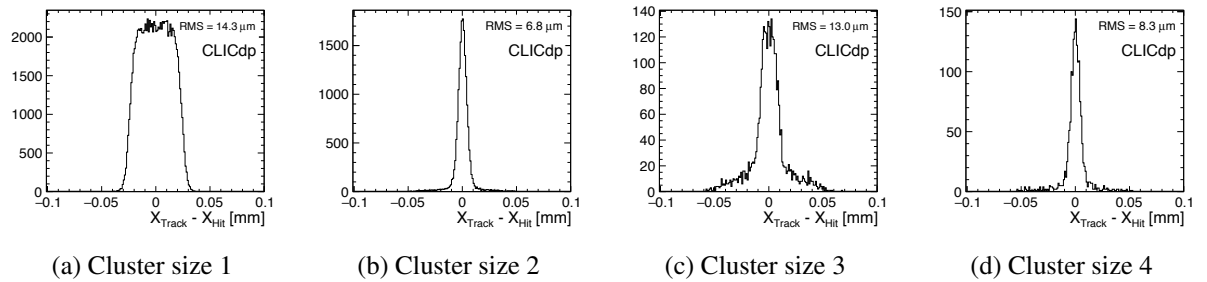

(a) Cluster size 1

(b) Cluster size 2

(c) Cluster size 3

(d) Cluster size 4

Figure 19: Example single-point *x* residuals for different cluster sizes of assembly L04-W0125 (100 μm p-in-n). The RMS is calculated within a range of ±40 μm about 0. a) Cluster size 1: (1×1). b) Cluster size 2: (1×2) and (2×1). c) Cluster size 3: (2×2). d) Cluster size 4 (2×2).

The overall residual of the assembly is the averaged residual of each cluster size, taking into account the relative fractions of different cluster sizes. Therefore, sensor thickness and operating conditions can

both affect the overall resolution of the assembly, as both these factors affect the fraction of cluster sizes (shown in Section 6.2). Under nominal operating conditions, the effect of sensor thickness is shown in Figure 20. Thinner sensors have a larger fraction of single-pixel clusters, contributing a wider component to the residual distribution (Figure 20(a)). As the thickness of the sensor increases, the fraction of more precisely reconstructed multi-pixel clusters increases which results in a narrower residual (Figure 20(d)). Under nominal operating conditions, the single-point residual as a function of sensor thickness is shown in Figure 21. As expected, as thicker sensors yield more multi-pixel clusters they achieve a smaller single-point resolution.
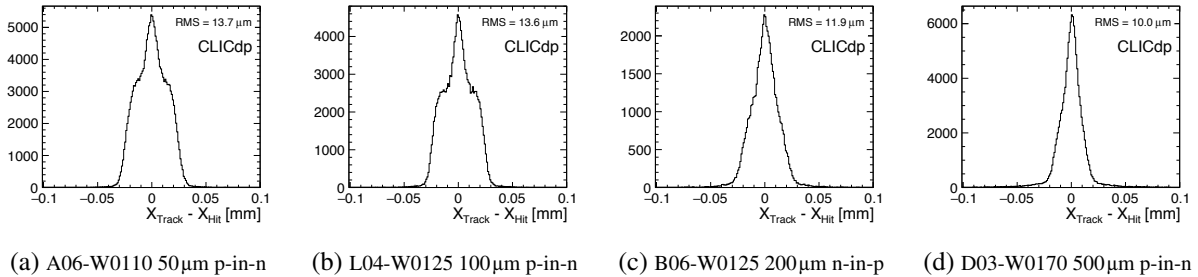

(a) A06-W0110 50 µm p-in-n   (b) L04-W0125 100 µm p-in-n   (c) B06-W0125 200 µm n-in-p   (d) D03-W0170 500 µm p-in-n

Figure 20: Example single-point *x* residuals for assemblies with silicon sensors of different thickness. The RMS is calculated within a range of $\pm 40\,\mu\text{m}$ about 0.
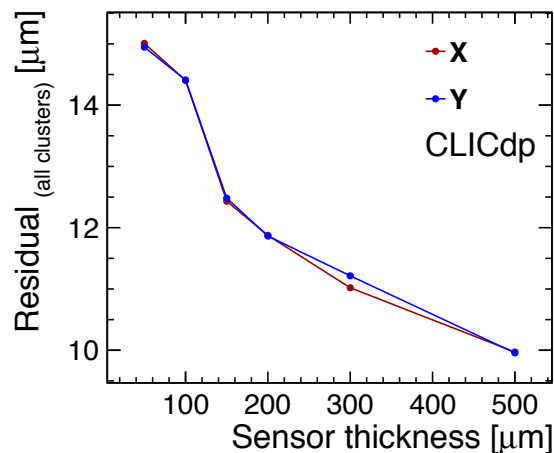

Figure 21: Single-point *x* and *y* residuals as a function of sensor thickness, using all available data. The average of the RMS calculated per run in a range of $\pm 40\,\mu\text{m}$ about 0 is used. The track resolution is not unfolded.

The distribution of different cluster sizes, and hence the resolution, can also be influenced by the operating conditions of the assembly. Figure 22 shows examples of this. The trend of these plots follows the behaviour of the fraction of single-pixel clusters, confirming that fewer single-pixel clusters results in a smaller residual.

Thus far, the single-point residuals have been measured using cluster positions calculated from TOT measurements. For calibrated assemblies, it is also possible to calculate the cluster position using energy measurements. For cluster shapes using the η-correction method, this results in a different optimal σ_{EC}. Figure 23 gives three comparisons between the single-point residuals of two-pixel clusters calculated
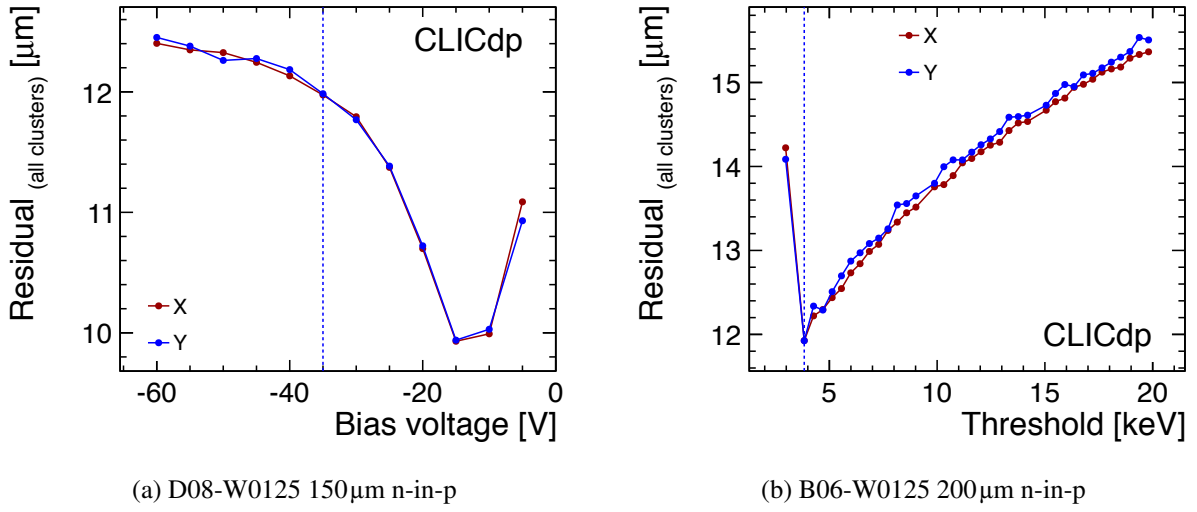
(a) D08-W0125 150 μm n-in-p

(b) B06-W0125 200 μm n-in-p

Figure 22: Single-point *x* and *y* residuals as a function of bias voltage (a) and threshold (b). The average of the RMS calculated per run in a range of ±40 μm about 0 is used. The nominal operating condition is shown by the blue dashed line. The track resolution is not unfolded.

using TOT, energy from global calibration constants and energy from pixel calibration constants [6]. It can be seen that calibrating the TOT measurements improves the single-point resolution minimally.
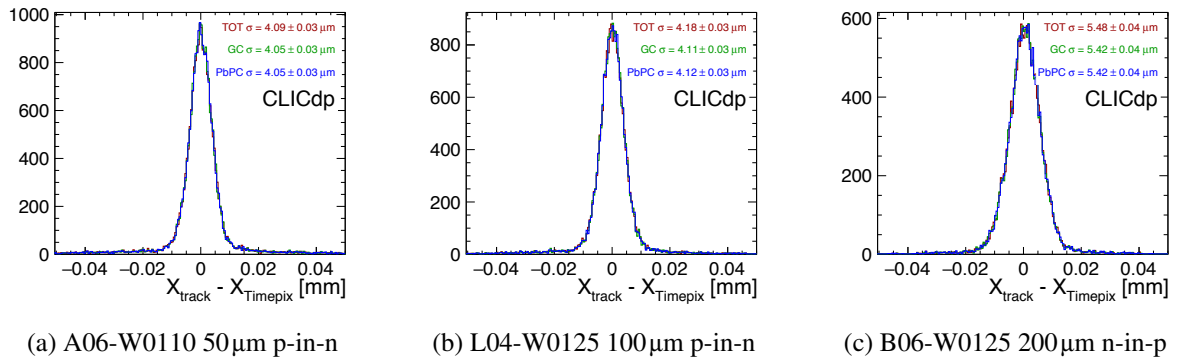

(a) A06-W0110 50 μm p-in-n

(b) L04-W0125 100 μm p-in-n

(c) B06-W0125 200 μm n-in-p

Figure 23: Single-point two-pixel cluster *x* residuals for three assemblies, where the hit position has been calculated using TOT (red), global calibrated energy (green) and pixel by pixel calibrated energy (blue). The σ parameter of a fitted Gaussian is used.

6.4. Detection efficiency

6.4.1. Global efficiency

The detection efficiency is calculated by counting the number of tracks matched to hits (within a window of radius 0.1 mm) and dividing by the total number of tracks which are projected to pass through the assembly. Efficiency measurements are calculated within the 256×256 pixels of the main sensor area for all assemblies, including those assemblies with active-edge technology. In this analysis neither masked pixels nor hot pixels are corrected for, meaning that a track passing through a masked or hot pixel and not being detected does contribute to an assembly's inefficiency.

The efficiency depends strongly on the threshold of the ASIC, as lowering the threshold makes it more likely that a deposited charge will be above threshold. This behaviour is seen in Figure 24, and in the results of additional assemblies presented in Figure 33 of Appendix C. A secondary feature of these plots is that as the threshold gets extremely low, the efficiency is seen to drop. This is caused by the increasing number of hot pixels at low thresholds, as shown in Figure 9(a). Most of the assemblies are seen to have excellent detection efficiency (in the range of 99-100%) for nominal operating thresholds, confirming that the nominal thresholds have been well chosen to balance charge collection with noise control. This includes both the assemblies with the $50 \mu m$ sensors, and the assemblies with the thinned $100 \mu m$ ASICs. Assemblies C07-W0125 and D09-W0126 are shown to have large inefficiencies. These inefficiencies are not accounted for by the number of masked and hot pixels, and are thought to be caused by operation or readout problems of the ASIC.
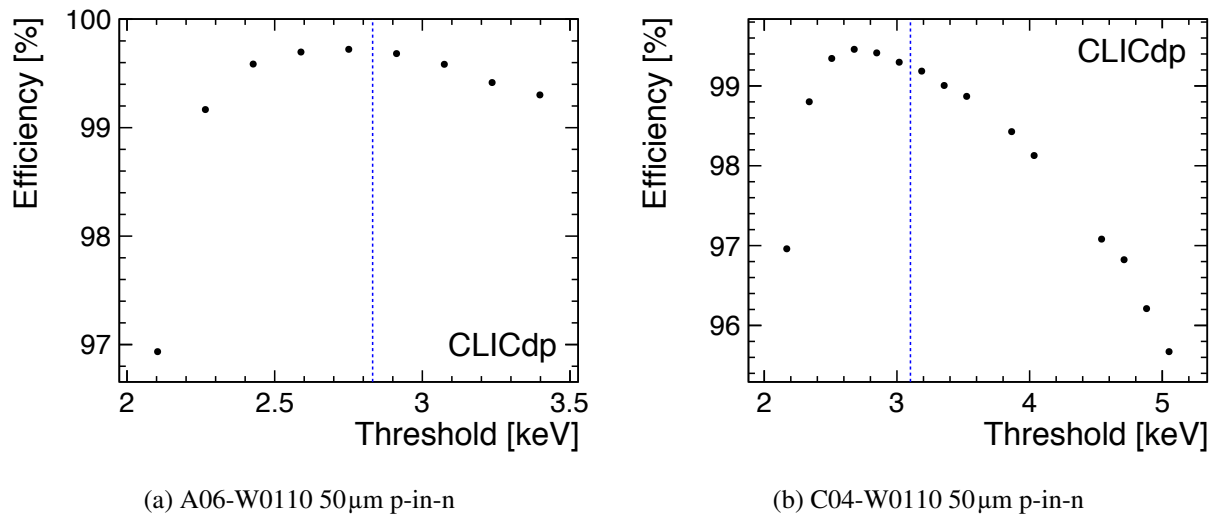

(a) A06-W0110 $50 \mu m$ p-in-n

(b) C04-W0110 $50 \mu m$ p-in-n

Figure 24: Detection efficiency as a function of operating threshold. The nominal operating condition is shown by the blue dashed line.

6.4.2. Edge efficiency

In addition to measuring the efficiency within the sensor area, the efficiency can be measured across the edge of the sensor. This is of particular interest for the assemblies with active-edge technology (see Section 2). Figure 25 shows a cross section of a $50 \mu m$ sensor with an active edge $20 \mu m$ wide. The active edge is achieved by continuing the implant on the backside of the sensor up the side wall of the sensor. Charge deposited in the edge can then be collected by the last pixel. The edge width (in this case $20 \mu m$) is measured from the edge of the implant in the final pixel. In the following analysis, the edge of the final pixel (i.e. $27.5 \mu m$ outside the centre of the final pixel) is taken as '0'. Results from two assemblies with active-edge technology are presented. The sensor with a $20 \mu m$ active edge has no guard ring, the sensor with a $50 \mu m$ active edge has one floating guard ring.

Data recorded under nominal operating conditions was used to measure the efficiency of the sensors across their edges. For this to be possible, it is necessary for tracks to be reconstructed in the region of the edge of the sensor. Due to the telescope geometry, at the DESY II test beam only two opposite edges were ever illuminated with reconstructible tracks. For the few runs recorded at the CERN PS test beam, the assembly was rotated by $90°$ with respect to the DESY II setup (see Section 4.3), hence the other two opposite sides were illuminated. Due to possible differences between each of the four edges of an assembly (guard ring position, width of the active edge, width of silicon until dicing position) each
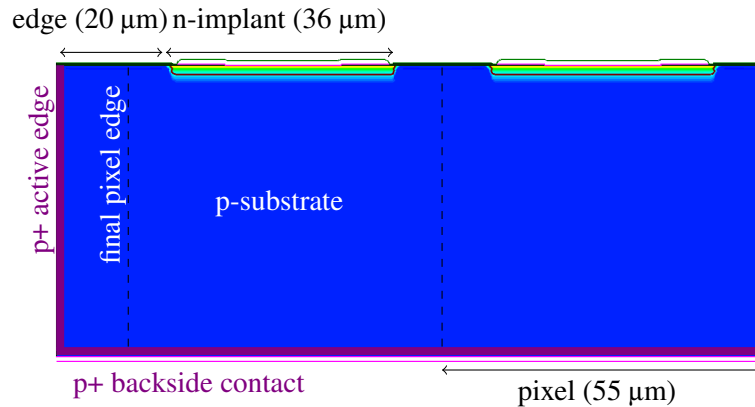
Figure 25: Schematic showing the cross section of a sensor with 20 µm active-edge technology. The pixel edges considered in the analysis are indicated with dashed lines.

edge is analysed separately. Edges are numbered $0 - 3$ clockwise around the assembly (as seen from the sensor side), starting with the edge closest to the periphery. In assemblies with active-edge technology it is expected that edge 0 behaves differently to the other three edges, as an extra row of pixels in the sensor next to the periphery prevents charge collection from this active edge.

The edge efficiency was analysed for all assemblies, combining together all runs recorded under nominal operating conditions. Figures 26(a) to 26(c) show the efficiency of the edges for three assemblies. For each edge it is also possible to calculate the measured TOT for each track as a function of position relative to the edge. This is presented in Figures 26(d) to 26(f).

Figures 26(a) and 26(d) show results for assembly C04-W0110, which has 50 µm active-edge technology. The efficiency in the region of edge 2 extends well past the expected edge of the last pixel. Moreover, the TOT measurements in the active-edge region match those from inside the sensor. This demonstrates successfully the active-edge technology in a 50 µm thick sensor. Figures 26(b) and 26(e) present results for assembly D04-W0125 which has a sensor 150 µm thick and no active edge. Again, significant efficiency is seen after the edge of the sensor for edge 2, however the measured TOT in this area is seen to be reduced compared to that measured inside the sensor. This is also explained by the extra row of pixels in the sensor next to the periphery. Finally, Figures 26(c) and 26(f) show results from assembly D03-W0170, which comprises a 500 µm thick sensor and no active edge. In both illuminated edges, significant efficiency is seen well past the expected edge. The measured TOT is seen to drop the further the track's position from the edge. It is thought that the thickness of this sensor allows charge collection via diffusion to occur. Additional results are presented in Figure 34 of Appendix C. Figures 34(a) and 34(d) show results from assembly A06-W0110, which has a 20 µm active edge. Despite low statistics, there is evidence of efficiency past the end of the last pixel in edges 2 and 3, without TOT loss. This matches the conclusions drawn from assembly C04-W0110.

6.5. Energy deposition

Six assemblies used during the test beams were also calibrated [6], meaning that the energy deposited in the sensor by traversing particles can be calculated by inverting Equation (1):

$$E = \frac{ta + \text{TOT} - b + \sqrt{(b + ta - \text{TOT})^2 + 4ac}}{2a} \, , \tag{5}$$

and applying the calibration constants shown in Table 4. Figure 27(a) shows the measured TOT distribution for assembly B06-W0125 (200 µm sensor) when operated under nominal conditions. Calibrating

(a) C04-W0110 50 μm p-in-n active edge

(b) D04-W0125 150 μm n-in-p slim edge

(c) D03-W0170 500 μm p-in-n slim edge

(d) C04-W0110 50 μm p-in-n edge 2

(e) D04-W0125 150 μm n-in-p edge 2
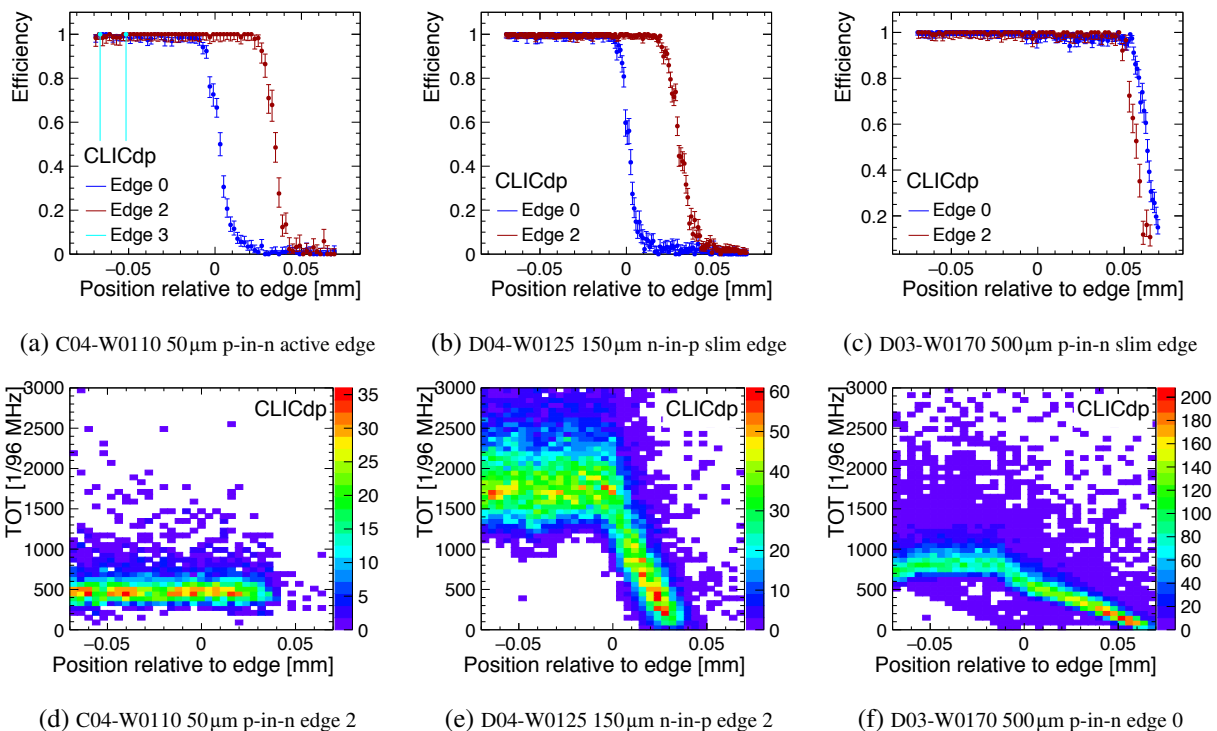
(f) D03-W0170 500 μm p-in-n edge 0

Figure 26: (a-c) The efficiency as a function of position relative to the edge for three different assemblies. (d-e) The measured TOT as a function of position relative to the edge for edges of interest in these three assemblies.

these TOT measurements using the global calibration constants determined for this assembly results in the energy distribution shown in Figure 27(b). This can be fitted with a Landau×Gauss convolution, where the Landau represents the energy deposition of a minimum ionising particle and the Gaussian accounts for the smearing caused by the resolution. The peak position (the most probable value of deposited energy in the sensor) can be identified by the μ parameter of the fitted Landau function.

Calibrating TOT measurements from all six possible assemblies, the most probable value of deposited energy as a function of sensor thickness is shown in Figure 27(c). As expected, the most probable value of deposited energy increases with sensor thickness approximately with the relationship [21]:

$$E_{\mathrm{MIP}}\,[\mathrm{eV}] = 80\,[\mathrm{e}^-/\mu\mathrm{m}] \times 3.6\,[\mathrm{eV/e}^-] \times T\,[\mu\mathrm{m}]\,, \tag{6}$$

where E_{MIP} is the expected most probable value of the energy deposited by a minimum ionising particle, and T is the thickness of the silicon sensor. The two 100 μm sensor assemblies are not in agreement with this prediction, nor are they consistent with each other. This behaviour was seen previously [6], and is not understood.

Under nominal operating conditions, the applied bias voltage ensures that the sensor is fully depleted and charge is collected from the total thickness. Reducing the bias voltage leads to under-depletion, when deposited charge is only collected from the depleted region. The collected energy as a function of bias voltage can be studied in order to calculate the depletion voltage of the sensor (the voltage at which the full thickness of the sensor is depleted). Figure 28 shows the most probable value of the collected energy as a function of bias voltage for three of the calibrated assemblies. By fitting the slope and the plateau regions of these plots, it is possible to estimate the depletion voltage of the assembly (the intersection of the two fitted lines). The bias scan results for the other three calibrated assemblies
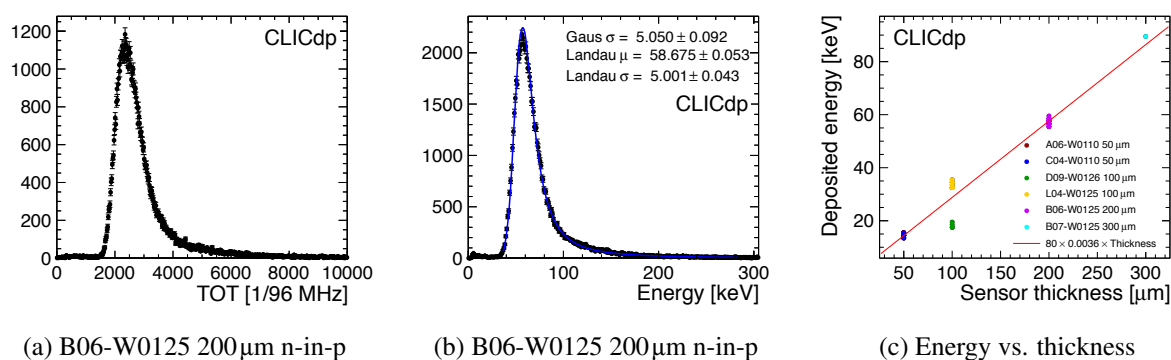
| (a) B06-W0125 200 μm n-in-p | (b) B06-W0125 200 μm n-in-p | (c) Energy vs. thickness |

Figure 27: a) The measured TOT distribution in a 200 μm silicon sensor. b) This TOT distribution calibrated using global calibration constants and fitted with a Landau×Gauss convolution. c) Most probable value of energy deposition as a function of sensor thickness per run for the calibrated assemblies, and compared with the expected value. All under nominal operating conditions.

are shown in Figure 35 of Appendix C. These scans did not allow the depletion voltage to be properly calculated. In the case of the two assemblies with 50 μm thick sensors, the bias voltage was never low enough to under deplete the sensors and the slope regions were not identified. In the case of assembly B07-W0125, the leakage current increased as the bias voltage increased and the plateau region was not identified. The calculated depletion voltages are presented in Table 8. First analysis of bias scan data samples were already presented in [22]. The results shown here are consistent with this study.

For those assemblies which were not calibrated, only TOT values are available. Nevertheless, the most probable value of measured TOT can be plotted against bias voltage, and the same behaviour of increasing TOT collection until the maximum is reached is seen (Figure 36 of Appendix C).

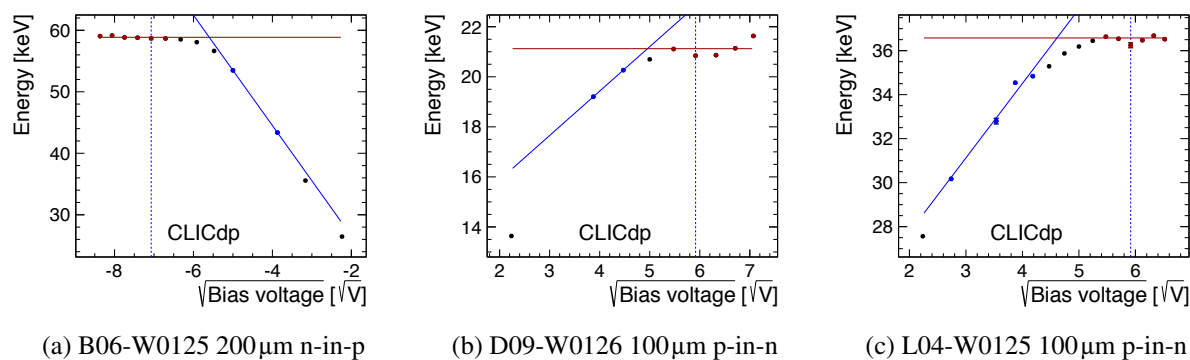| (a) B06-W0125 200 μm n-in-p | (b) D09-W0126 100 μm p-in-n | (c) L04-W0125 100 μm p-in-n |

Figure 28: Most probable value of deposited energy as a function of bias voltage for three calibrated assemblies. The slope and plateau regions are fitted with straight lines. The nominal operating condition is shown by the blue dashed line.

7. Summary

The performance of thin silicon sensors was investigated in test beam using Timepix readout ASICs. Silicon sensors of thickness $50-500$ μm were characterised. Data taking with the assemblies was successfully integrated with the acquisition of data from the EUDET beam telescope, and the recorded data

Table 8: Depletion voltage of the six calibrated assemblies, calculated by fitting the plateau and slope regions of energy as a function of bias voltage.

Assembly	Sensor thickness [μm]	Sensor type	Depletion voltage [V]
A06-W0110	50	p-in-n	≤ 15
C04-W0110	50	p-in-n	≤ 15
D09-W0126	100	p-in-n	25
L04-W0125	100	p-in-n	21
B06-W0125	200	n-in-p	-31
B07-W0125	300	p-in-n	≥ 20

samples were reconstructed to take the alignment of the assembly within the telescope into account.

Assemblies with sensors of all thicknesses were shown to have excellent detection efficiency - usually well over 99% under nominal operating conditions. Sensors with active-edge technology were also tested for efficiency in the edge region, and were shown to continue detecting hits with no loss of charge, leading to an efficiency in the active-edge region comparable to that inside the sensor. Previously determined calibrations for certain assemblies enabled energy deposition measurements. In most cases, the measured energy deposited in the sensors was in agreement with theoretical expectations. Bias voltage scans allowed the depletion voltages of several sensors to be determined. The single-point residual of each assembly was measured and shown to be highly dependent on the fraction of multi-pixel clusters, and therefore on the level of charge sharing within the sensor. For this reason, the single-point residual decreases as sensor thickness increases. Calibrated energy measurements were used to calculate the hit positions, but this did not lead to an improvement in resolution when compared to hit positions calculated with TOT measurements.

In conclusion, the detection efficiency of ultra-thin hybrid pixel detector assemblies with Timepix readout ASICs was shown to be compatible with that required for the CLIC vertex detector. However, the single-point resolution is strongly dependent on the level of charge sharing, which does not favour the thin sensors anticipated for CLIC. The detailed results reported in this note will be used to validate simulation models of pixel sensors. These models will guide the technology choice for the CLIC vertex detector. For example, the effect of reducing the pixel size from $55\,\mu m \times 55\,\mu m$ to $25\,\mu m \times 25\,\mu m$ can be studied through such simulations.

8. Acknowledgements

References

[1] M. Aicheler et al.,
A Multi-TeV Linear Collider Based on CLIC Technology: CLIC Conceptual Design Report,

CERN-2012-007. SLAC-R-985. KEK-Report-2012-1. PSI-12-01. JAI-2012-001 (2012),
URL: https://cds.cern.ch/record/1500095.

[2] L. Linssen et al., *Physics and Detectors at CLIC: CLIC Conceptual Design Report*,
arXiv:1202.5940. CERN-2012-003. ANL-HEP-TR-12-01. DESY-12-008. KEK-Report-2011-7
(2012), URL: https://cds.cern.ch/record/1425915.

[3] D. Dannheim, On behalf of the CLICdp collaboration, *The CLIC Vertex Detector*,
CLICdp-Conf-2014-009 (2014), URL: https://cds.cern.ch/record/1975520.

[4] G. Blanchot, D. Dannheim, C. Fuentes, On behalf of the CLICdp collaboration,
Power-pulsing schemes for vertex detectors at CLIC, JINST **9** CLICdp-Conf-2013-005 (2014),
URL: https://cds.cern.ch/record/1635206.

[5] X. Llopart et al., *Timepix, a 65k programmable pixel readout chip for arrival time, energy and/or
photon counting measurements*, NIM **A 581** (2007).

[6] N. Alipour Tehrani et al.,
Calibration of ultra-thin hybrid pixel detector assemblies with Timepix readout ASICs,
CLICdp-Note-2015-003 (2015), URL: http://cds.cern.ch/record/2054922.

[7] J. Jakubek et al., *Pixel detectors for imaging with heavy charged particles*, NIM **A 591** (2008).

[8] I. Rubinskiy, *An EUDET/AIDA Pixel Beam Telescope for Detector Development*,
Physics Procedia **37** (2012), Proceedings of the 2nd International Conference on Technology and
Instrumentation in Particle Physics (TIPP 2011).

[9] C. Hu-Guo et al., *First reticle size MAPS with digital output and integrated zero suppression for
the EUDET-JRA1 beam telescope*, NIM A **623** (2010).

[10] H. Perrey,
EUDAQ and EUTelescope: Software Frameworks for Test Beam Data Acquisition and Analysis,
PoS **TIPP2014** (2014), Proceedings of the 3rd International Conference on Technology and
Instrumentation in Particle Physics (TIPP 2014).

[11] T. Behnke et al., *Test Beams at DESY*, EUDET-Memo-2007-11 (2007), URL:
http://www.eudet.org/e26/e28/e182/e283/eudet-memo-2007-11.pdf.

[12] V. Kraus et al., *FITPix – fast interface for Timepix pixel detectors*, JINST **6** (2011).

[13] *Man in the middle trigger logic unit*,
URL: http://svnweb.cern.ch/world/wsvn/MIMTLU.

[14] I. Rubinskiy, *EUTelescope. Offline track reconstruction and DUT analysis software.*
EUDET-Memo-2010-12 (2010), URL: http://www.eudet.org/e26/e28/e86887/e107460/EUDET-Memo-2010-12.pdf.

[15] *pyEudetAnalysis*,
URL: https://github.com/pyEudetAnalysis/pyEudetAnalysis.

[16] F. Gaede, *Marlin and LCCD: Software tools for the ILC*, Nucl. Instrum. Meth. **A559** (2006),
Proceedings of the 10th International Workshop on Advanced computing and analysis techniques
in physics research, ACAT05, Zeuthen, Germany, May 22-27, 2005.

[17] *SciPy hierarchical fclusterdata*, URL: http://docs.scipy.org/doc/scipy/reference/generated/scipy.cluster.hierarchy.fclusterdata.html.

[18] E. Belau et al., *Charge collection in silicon strip detectors*, NIM **214** (1983).

[19] *SciPy optimize minimize*, URL: http://docs.scipy.org/doc/scipy/reference/generated/scipy.optimize.minimize.html.

[20] F. Hartmann, *Evolution of silicon sensor technology in particle physics*,
      Springer tracts in modern physics, Springer, Berlin, 2009,
      URL: http://cds.cern.ch/record/1100830.

[21] G. F. Knoll, *Radiation detection and measurement; 4th ed.* Wiley, New York, NY, 2010,
      URL: https://cds.cern.ch/record/1300754.

[22] S. Maimon, S. Redford, *Analysis of bias voltage scan data recorded with hybrid Timepix1 silicon
      pixel assemblies at the DESY testbeam*, LCD-OPEN-2014-001 (2014).

A. Assembly Characterisation Appendix

Figure 29 shows the masked pixel maps for all assemblies except assembly L04-W0125. This can be found in Figure 1.
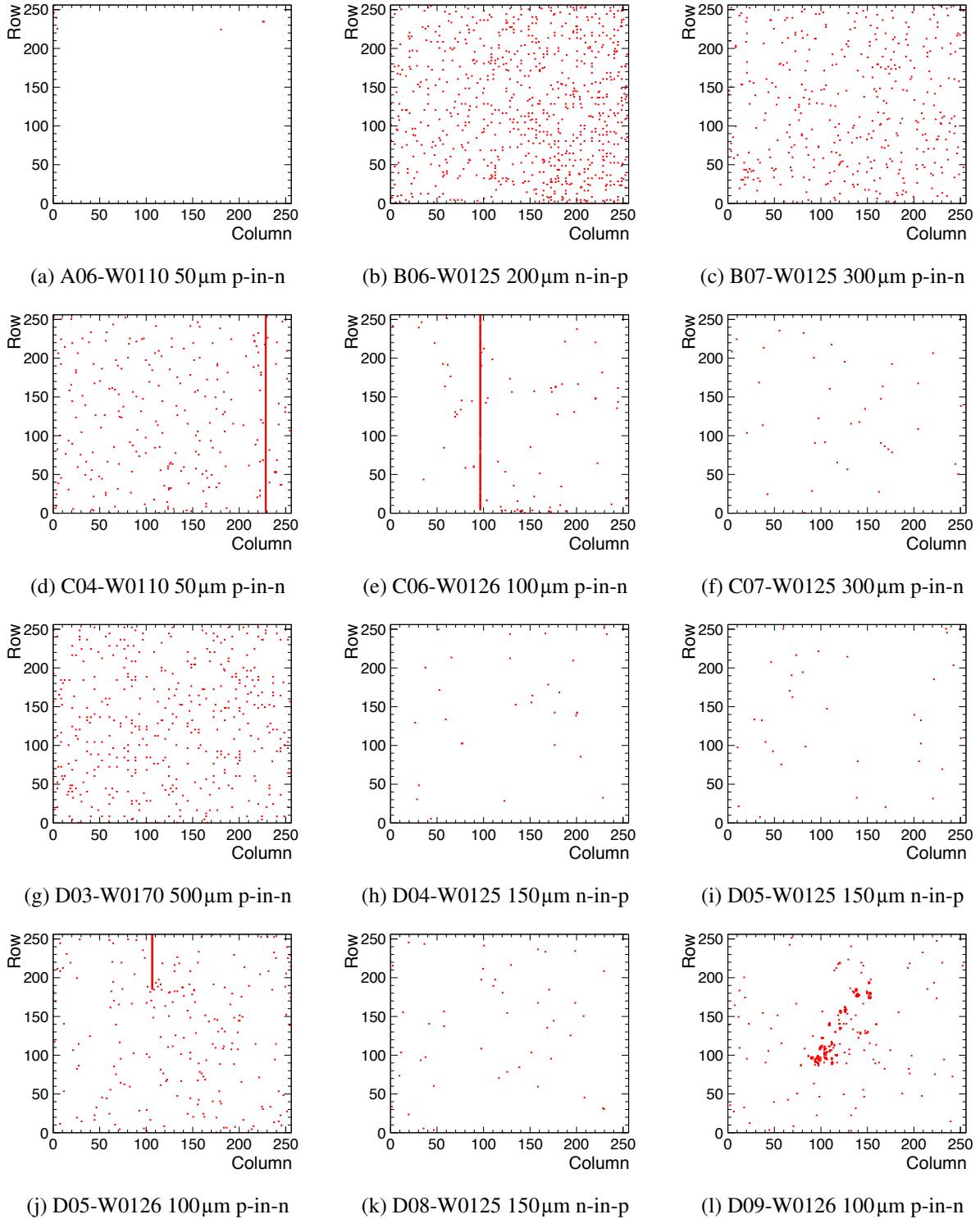

(a) A06-W0110 50 μm p-in-n

(b) B06-W0125 200 μm n-in-p

(c) B07-W0125 300 μm p-in-n

(d) C04-W0110 50 μm p-in-n

(e) C06-W0126 100 μm p-in-n

(f) C07-W0125 300 μm p-in-n

(g) D03-W0170 500 μm p-in-n

(h) D04-W0125 150 μm n-in-p

(i) D05-W0125 150 μm n-in-p

(j) D05-W0126 100 μm p-in-n

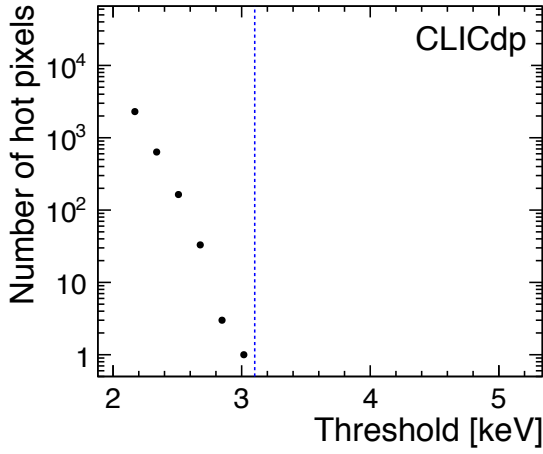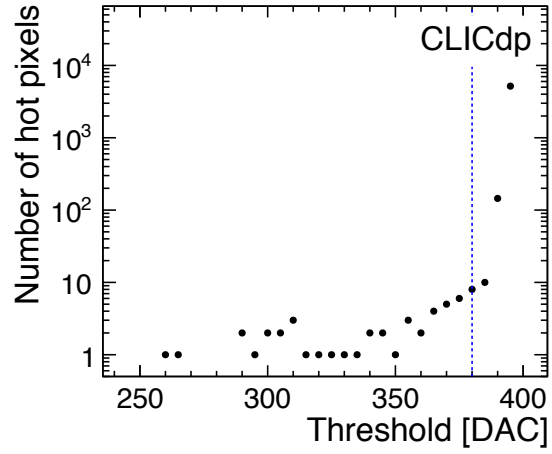(k) D08-W0125 150 μm n-in-p

(l) D09-W0126 100 μm p-in-n

Figure 29: Masked pixel maps.
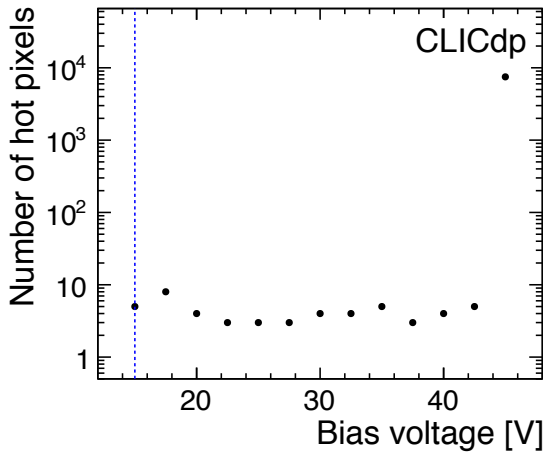
B. Reconstruction and Data Samples Appendix

Figure 30 shows examples of how the number of hot pixels found depends on the operating conditions in the Timepix. Other examples can be found in Figure 9.
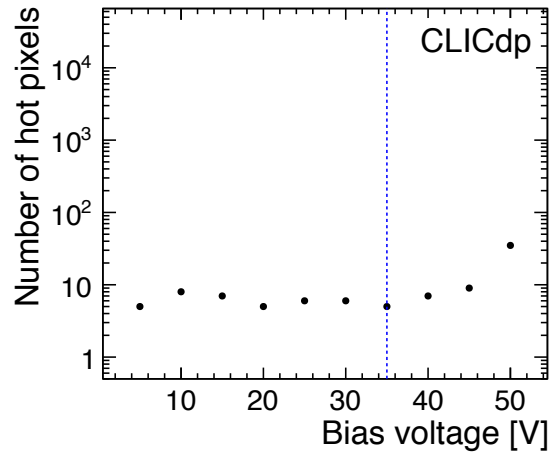

(a) C04-W0110 50 μm p-in-n

(b) C06-W0126 100 μm p-in-n

(c) A06-W0110 50 μm p-in-n

(d) C06-W0126 100 μm p-in-n

Figure 30: The number of hot pixels as a function of operating threshold (a,b) and bias voltage (c,d). The nominal operating condition is shown by the blue dashed line.

C. Experimental Results Appendix

Figure 31 shows examples of how the distribution of cluster sizes varies with the operating conditions of the assembly. Further plots can be found in Figure 18.

(a) C06-W0126 100 μm p-in-n

(b) B06-W0125 200 μm n-in-p

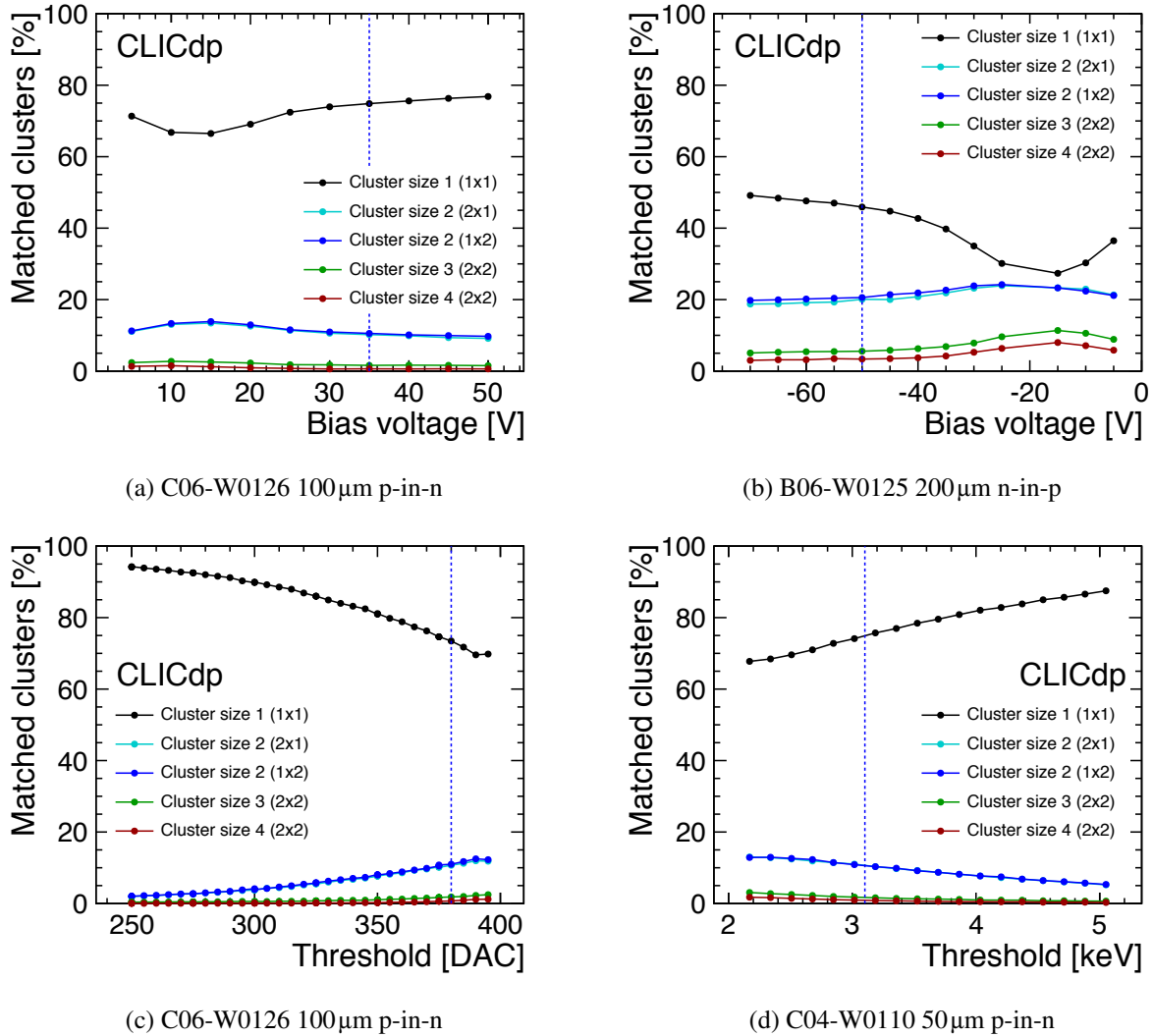(c) C06-W0126 100 μm p-in-n

(d) C04-W0110 50 μm p-in-n

Figure 31: Fraction of different cluster sizes as a function of bias voltage (a, b) and threshold (c, d). The nominal operating condition is shown by the blue dashed line.

Figure 32 shows track position within the pixel, for cluster size $1 - 4$ and as a function of sensor thickness. The plots for assembly L04-W0125 are also shown in Figure 15.

(a) 50 μm cluster size 1   (b) 50 μm cluster size 2   (c) 50 μm cluster size 3   (d) 50 μm cluster size 4

(e) 100 μm cluster size 1   (f) 100 μm cluster size 2   (g) 100 μm cluster size 3   (h) 100 μm cluster size 4

(i) 150 μm cluster size 1   (j) 150 μm cluster size 2   (k) 150 μm cluster size 3   (l) 150 μm cluster size 4

(m) 200 μm cluster size 1   (n) 200 μm cluster size 2   (o) 200 μm cluster size 3   (p) 200 μm cluster size 4

(q) 500 μm cluster size 1   (r) 500 μm cluster size 2   (s) 500 μm cluster size 3   (t) 500 μm cluster size 4
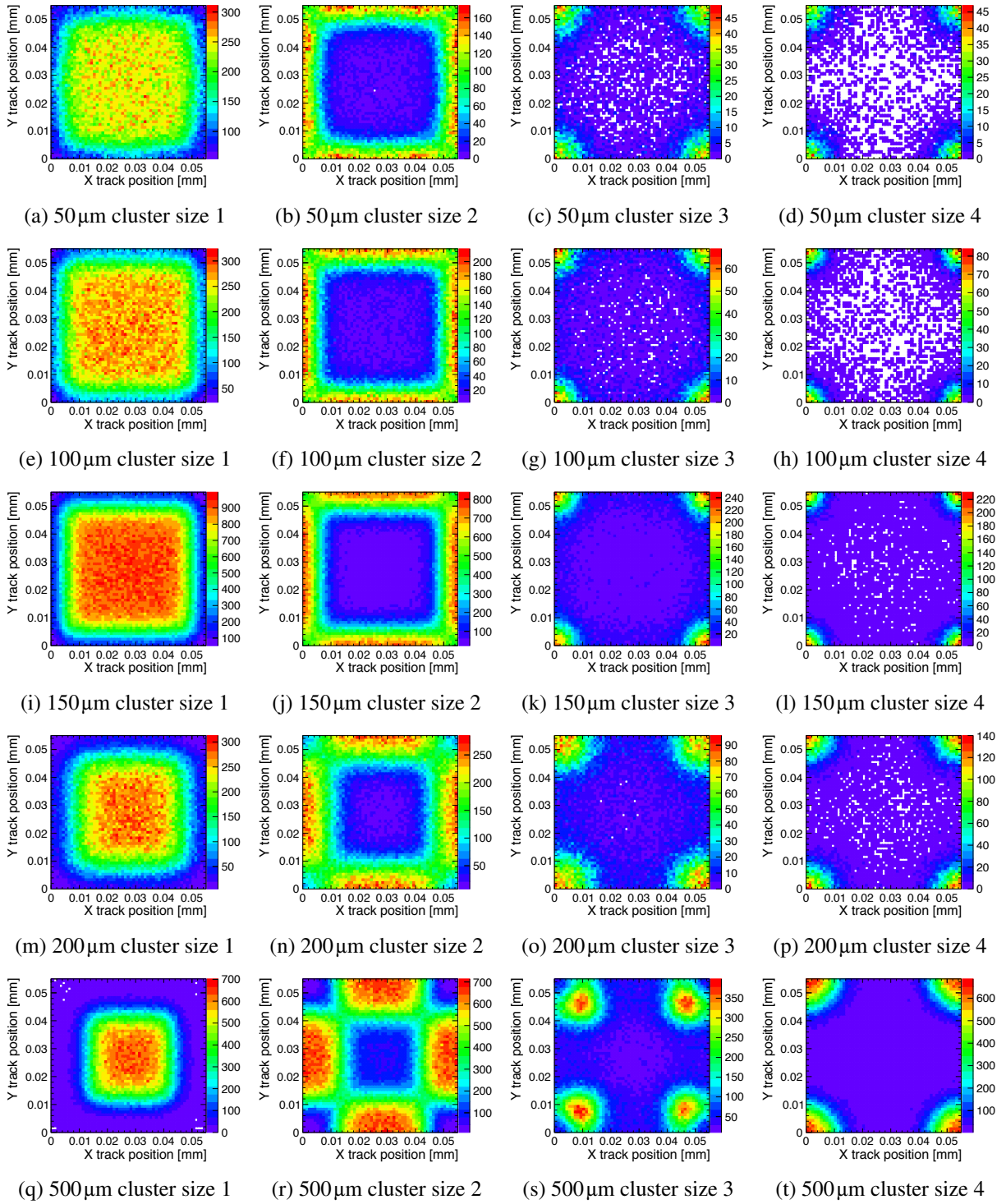
Figure 32: Track position in the pixel for cluster sizes 1 − 4, recorded under nominal operating conditions. Assemblies used, in order of increasing thickness: A06-W0110, L04-W0125, D04-W0125, B06-W0125, D03-W0170.

31

Figure 33 shows examples of how the detection efficiency varies with the operating threshold. Further plots can be found in Figure 24.

(a) B06-W0125 200 µm n-in-p

(b) C06-W0126 100 µm p-in-n

(c) C07-W0125 300 µm p-in-n

(d) D04-W0125 150 µm n-in-p

(e) D05-W0125 150 µm n-in-p

(f) D05-W0126 100 µm p-in-n

(g) D08-W0125 150 µm n-in-p

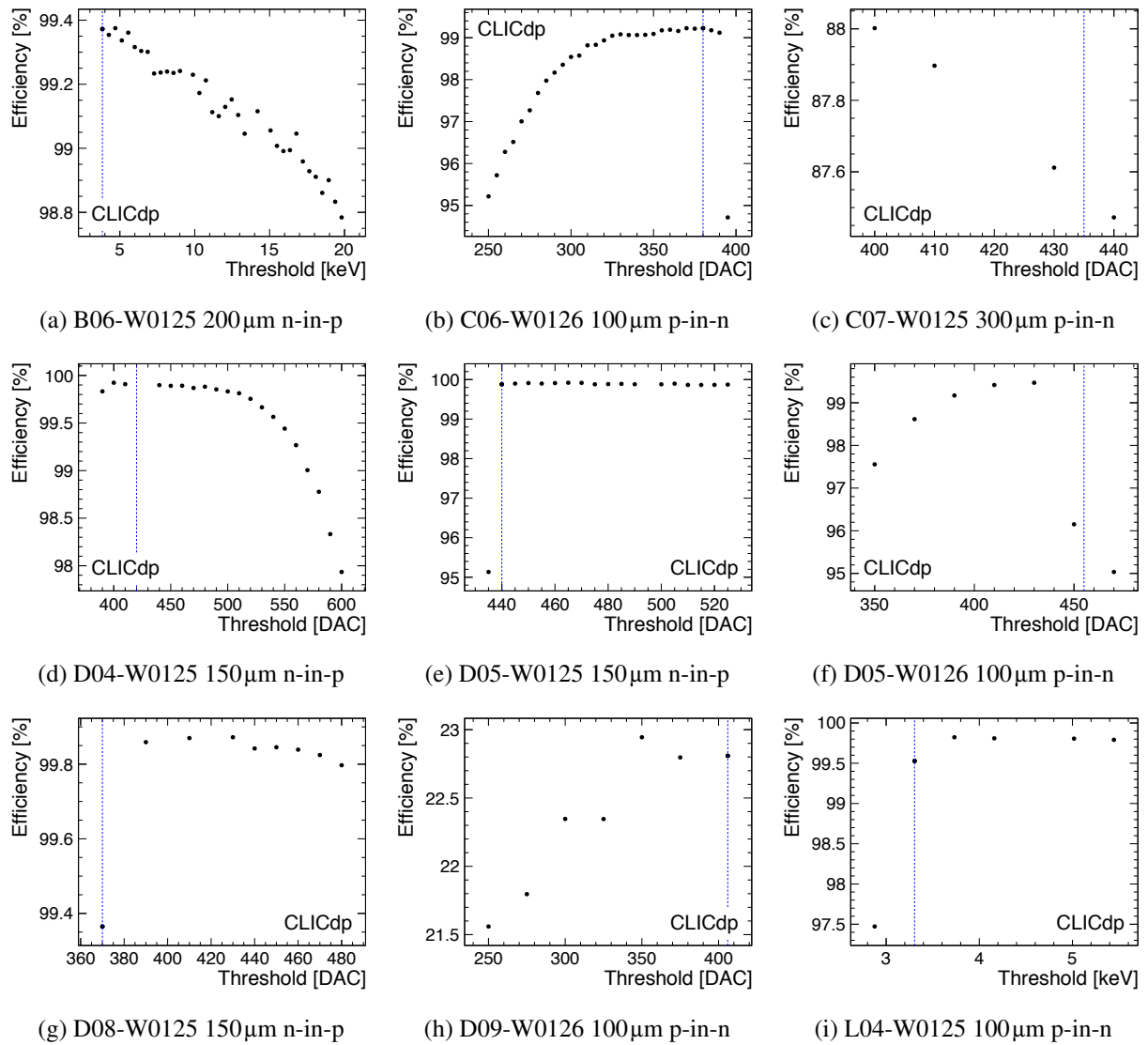(h) D09-W0126 100 µm p-in-n

(i) L04-W0125 100 µm p-in-n

Figure 33: Detection efficiency as a function of operating threshold. The nominal operating condition is shown by the blue dashed line.

Figure 34 shows examples of assembly efficiencies in the edge region, and the measured TOT values as a function of position relative to the edge. Further examples can be seen in Figure 26.

(a) A06-W0110 50 μm p-in-n active edge

(b) B06-W0125 200 μm n-in-p slim edge

(c) D08-W0125 150 μm n-in-p slim edge

(d) A06-W0110 50 μm p-in-n edge 2

(e) B06-W0125 200 μm n-in-p edge 0
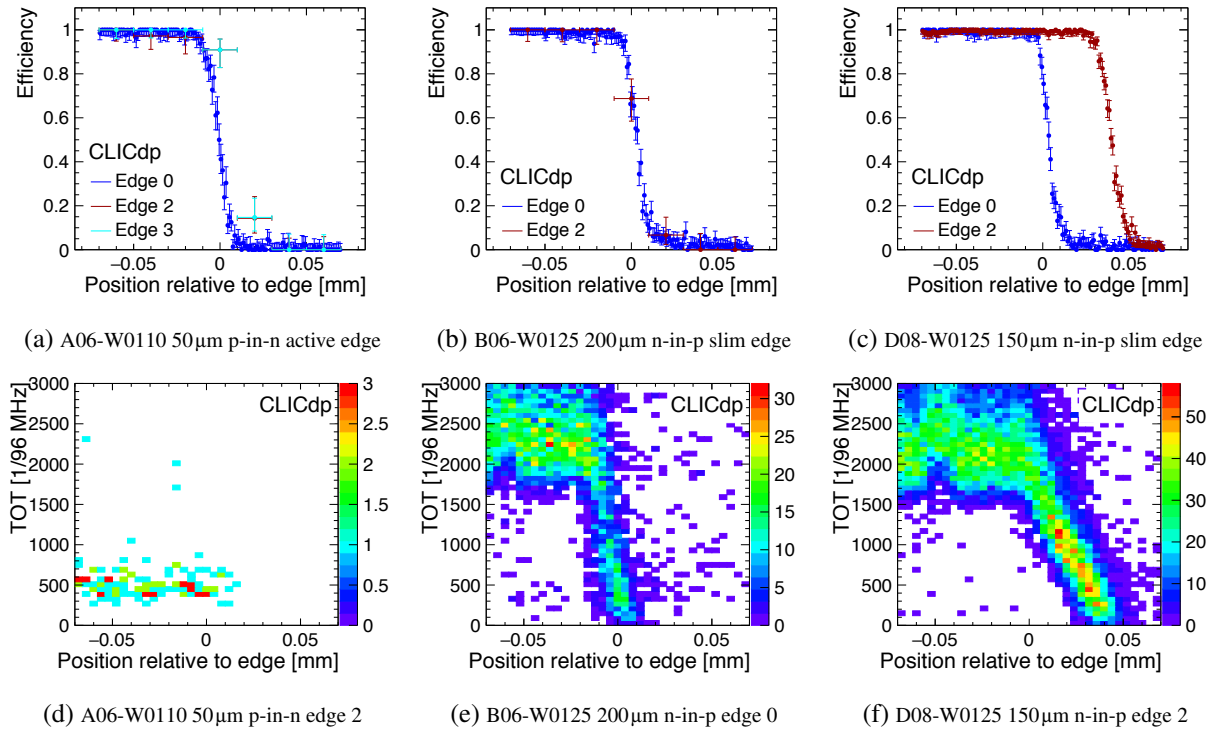

(f) D08-W0125 150 μm n-in-p edge 2

Figure 34: (a-c) The efficiency as a function of position relative to the edge for three different assemblies. (d-e) The measured TOT as a function of position relative to the edge for edges of interest in these three assemblies.

Figure 35 shows the energy deposition as a function of bias three calibrated assemblies. The results for the other three calibrated assemblies are shown in Figure 28.

(a) A06-W0110 50 μm p-in-n

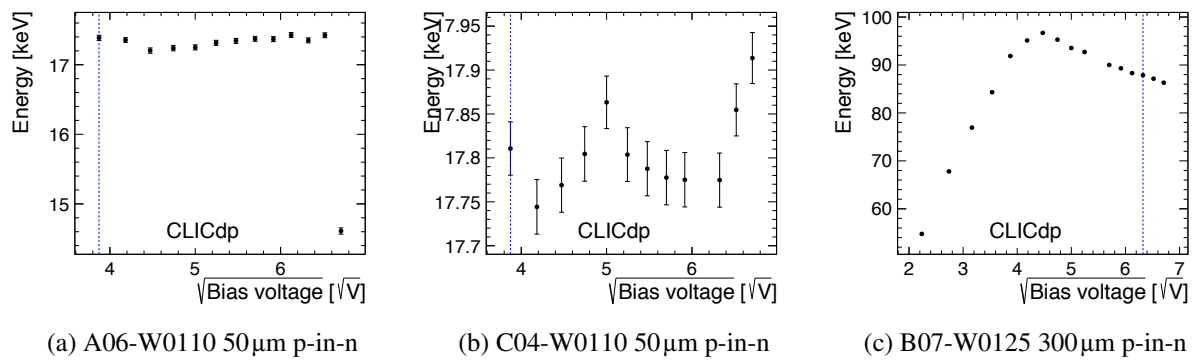(b) C04-W0110 50 μm p-in-n

(c) B07-W0125 300 μm p-in-n

Figure 35: Most probable value of deposited energy as a function of bias voltage for three calibrated assemblies. The nominal operating condition is shown by the blue dashed line.

Figure Figure 36 shows the behaviour of measured TOT as a function of bias voltage, for those assemblies which were not calibrated. Calibrated assemblies are shown in Figure 28.

(a) C06-W0126 100 μm p-in-n

(b) C07-W0125 300 μm p-in-n

(c) D03-W0170 500 μm p-in-n

(d) D04-W0125 150 μm n-in-p

(e) D05-W0125 150 μm n-in-p

(f) D05-W0126 100 μm p-in-n
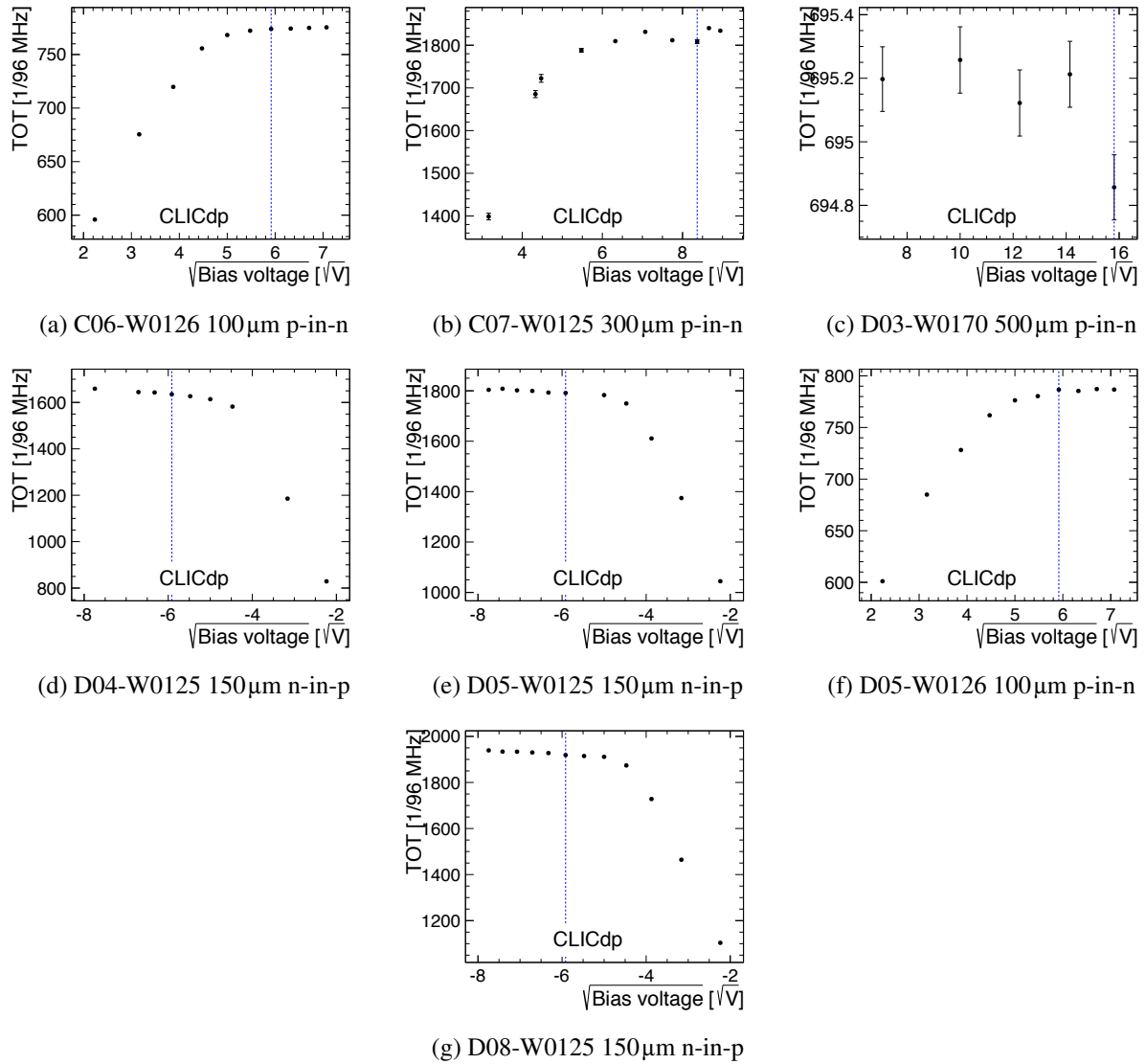
(g) D08-W0125 150 μm n-in-p

Figure 36: Most probable value of measured TOT as a function of bias voltage for assemblies which were not calibrated. The TOT spectrum of single-pixel clusters only is used. The nominal operating condition is shown by the blue dashed line.